AIMS Mathematics, 11(3): 8546–8583.
DOI: 10.3934/math.2026352
Received: 02 January 2026
Revised: 07 March 2026
Accepted: 12 March 2026
Published: 30 March 2026

Mathematics

https://www.aimspress.com/journal/Math

Research article

A unified fractional-stochastic energy balance model: Theoretical analysis, numerical implementation, and implications for sustainable energy systems

Kinda Abuasbeh[1] **and Salma Trabelsi**[2,*]

[1] Department of Robotics and Control Engineering, College of Engineering, Al Zaytoonah University of Science and Technology, Salfit, P390, Palestine

[2] Department of Mathematics, College of Science, King Faisal University, P.O. Box 400, Al-Ahsa, 31982, Saudi Arabia

* **Correspondence:** Email: satrabelsi@kfu.edu.sa.

Abstract: Modeling climate-energy interactions requires frameworks that capture both long-range memory and extreme event risks. Classical energy balance models (EBMs) are limited by their memoryless deterministic structure, while purely stochastic extensions typically incorporate only Gaussian noise and fail to account for heavy-tailed extremes. This paper introduces a unified fractional-stochastic energy balance equation (FS-EBE) that combines Caputo fractional integrals for memory effects with Lévy processes for stochastic forcing, including jumps. We establish the model's well-posedness by proving existence, uniqueness, and moment boundedness for the resulting stochastic Volterra equation. A dedicated fractional-stochastic Adams-Bashforth-Moulton (ABM) predictor-corrector scheme is developed for a numerical solution. Through two case studies—periodic solar forcing with Gaussian noise and correlated forcing with Lévy jumps—we demonstrate that the FS-EBE produces phase lags, long-tailed relaxation following extremes, and heavier-tailed anomaly distributions absent in classical and standard stochastic EBMs. Two novel indices are introduced: the fractional memory index ($M = 1 - \alpha$) quantifying system memory and the stochastic fractional robustness index (SFRI) measuring finite-time resilience. These provide quantitative tools for assessing energy infrastructure vulnerability to climate extremes, supporting Sustainable Development Goal 7 affortable and clean energy.

Keywords: fractional calculus; stochastic energy balance; Lévy processes; climate-energy modeling; eesilience index; energy system reliability
Mathematics Subject Classification: 35R11, 60H10, 86A10, 90B25, 93E03

1. Introduction

The reliability, resilience, and safety of modern energy systems are inextricably linked to the complex dynamics of Earth's climate [28, 40]. Climate variability introduces profound uncertainties in renewable generation and imposes extreme stresses on energy infrastructure [28]. Consequently, quantifying climate-driven risks is essential for planning resilient energy grids [38].

Traditional risk assessment frameworks rely on stationary statistics or deterministic simulations, but these approaches inadequately capture two defining characteristics of the climate-energy nexus: long-range temporal memory and non-Gaussian extreme events [12, 21]. Classical energy balance models (EBMs), which describe global temperature via first-order ordinary differential equations, epitomize these limitations. Their memoryless, deterministic structure fails to account for slow-response components like ocean heat uptake [19] and underestimates tail risks from events such as volcanic eruptions or persistent droughts [42, 45]. The mathematical foundations for modeling such phenomena draw on Lévy process theory [1, 22] and stochastic analysis [16, 33], with Gronwall-type inequalities [7] essential for stability.

Reliability engineering has developed sophisticated models for similar challenges. Recent work addresses non-stationary extremes [5], system deterioration via stochastic differential (SDEs) [20], and structural health monitoring [48]. Resilience frameworks quantify infrastructure performance under stress [8], with applications to power grids under typhoons [27], hurricane impacts [40]. Metamaterials research [6]. While multi-dimensional resilience assessment [37] provides tools for evaluating electric power systems subject to hurricanes.

Fractional calculus provides a natural framework for modeling memory and hereditary phenomena [25, 32, 39]. Applications include probabilistic failure analysis of structures with fractional elements [3], comprehensive reviews of fractional methods [18], spectral estimation techniques [43], and path integral approaches for nonlinear systems [15]. Numerical methods for fractional equations rely on predictor-corrector schemes [13]. The characterization of temperature variability through scaling and intermittency [29, 41] provides important context for understanding the multi-scale nature of climate fluctuations.

Despite these advances, a critical disconnect remains. Climate models for energy system studies have not kept pace with engineering models. Stochastic EBMs typically incorporate only Gaussian noise [14, 23, 34, 35], missing heavy-tailed extremes, while general circulation models [44] are computationally prohibitive for ensemble-based risk assessment. What is lacking is a unified model integrating long-memory via fractional operators and non-Gaussian stochasticity via Lévy processes within a mathematically rigorous framework amenable to reliability analysis.

Recent developments address these gaps from different angles. Non-Markovian energy balance models naturally yield fractional formulations [46]. Numerical methods for fractional reaction-diffusion systems [30, 47] demonstrate growing computational sophistication. Power system dynamics benefit from higher-order approximations [24], and spatiotemporal statistical methods [36] inform regional climate-energy assessments.

While this manuscript was under review, Awadalla and Sharif [2] published a significant contribution applying fractional calculus to energy balance modeling. Their work validates fractional memory using Caputo derivatives and demonstrates improved historical temperature reconstruction. However, their model remains deterministic and focuses on climate science applications. Our work

differs fundamentally in three respects that directly address reviewer questions about novelty. First, we employ Caputo fractional integrals (Riemann-Liouville type) rather than derivatives. This distinction is physically meaningful: Fractional derivatives model anomalous rates of change, while fractional integrals represent cumulative weighted memory of past states, directly analogous to energy storage in oceans and ice sheets. Second, we incorporate Lévy processes, enabling the model to generate both continuous Gaussian variability and discontinuous extreme events essential for energy system risk assessment, where tail events drive infrastructure failures. Third, while [2] validates against historical temperature records, we introduce novel resilience indices specifically designed for energy system planning: The fractional memory index ($M = 1 - \alpha$) quantifying system memory and the stochastic fractional robustness index (SFRI) measuring finite-time resilience as practical tools for assessing infrastructure vulnerability to climate extremes.

This paper bridges this gap by introducing a unified fractional-stochastic energy balance equation (FS-EBE). The proposed model advances the state-of-the-art by combining fractional integrals with Lévy processes in an EBM context, which enables simultaneous modeling of long memory and extreme events; providing a physical reinterpretation through fractional integrals representing cumulative energy storage in slow-response climate components; establishing mathematical foundations for the stochastic case by proving existence, uniqueness, and moment boundedness for stochastic Volterra equations with Lévy noise, which extends deterministic results to the stochastic regime; introducing novel resilience metrics as practical tools for energy infrastructure planning; and developing a dedicated fractional-stochastic Adams-Bashforth-Moulton (ABM) predictor-corrector method that handles both hereditary integrals and Lévy increments.

The remainder of this paper is organized as follows. Section 2 reviews mathematical preliminaries. Section 3 introduces the FS-EBE and its physical interpretation. Section 4 establishes existence, uniqueness, and stability. Section 5 details the numerical scheme. Section 6 describes simulation setup and case studies. Section 7 presents results and comparative analysis. Section 8 discusses implications for energy system reliability, and Section 9 concludes.

2. Mathematical preliminaries

This section reviews the essential mathematical concepts underpinning the unified FS-EBE. All definitions and theorems are cited from the established literature.

2.1. Fractional calculus

Definition 2.1 (Riemann-Liouville fractional integral)**.** *For a function $f \in L^1([0,T])$ and order $\alpha > 0$, the Riemann-Liouville fractional integral is defined as*

$$ {}_0I_t^\alpha f(t) = \frac{1}{\Gamma(\alpha)} \int_0^t (t-\tau)^{\alpha-1} f(\tau) d\tau, \tag{2.1} $$

where $\Gamma(\cdot)$ is the Euler Gamma function [25, 32].

The Riemann-Liouville integral is a linear operator and satisfies the semigroup property, ${}_0I_t^\alpha \circ {}_0I_t^\beta f(t) = {}_0I_t^{\alpha+\beta} f(t)$ for $\alpha, \beta > 0$ [25].

Definition 2.2 (Caputo fractional derivative)**.** *For a function f absolutely continuous on $[0, T]$ and $n - 1 < \alpha < n$, the Caputo fractional derivative is defined as*

$$ {}_0^C D_t^\alpha f(t) = {}_0 I_t^{n-\alpha} \left(\frac{d^n f(t)}{dt^n} \right) = \frac{1}{\Gamma(n-\alpha)} \int_0^t (t-\tau)^{n-\alpha-1} f^{(n)}(\tau) d\tau, \tag{2.2} $$

with $n = \lceil \alpha \rceil$ [25, 32, 39].

Fractional calculus has also been successfully applied across diverse scientific domains, demonstrating its versatility in modeling memory and hereditary phenomena. In fluid mechanics, fractional models capture anomalous diffusion and viscoelastic behavior in complex flows [26]. In mathematical biology, fractional operators describe memory effects in biological tissues and predator-prey dynamics [17, 31]. In image processing, fractional diffusion equations have proven effective for noise removal [4, 9] and super-resolution reconstruction [10, 11]. These interdisciplinary applications underscore the broad utility of fractional calculus and motivate its use in the present climate-energy framework.

Remark 2.3 (Fractional integral vs derivative)**.** *Throughout this paper, we employ the Caputo fractional integral of order $\alpha > 0$, denoted ${}_0^C D_t^{-\alpha}$, which coincides with the Riemann-Liouville fractional integral ${}_0 I_t^\alpha$ defined in Definition 2.1. This operator represents the cumulative weighted memory of past states and is distinct from the Caputo fractional derivative (Definition 2.2), which captures anomalous rates of change. Our model uses the fractional integral, not the derivative, to represent memory effects. For comprehensive treatments of fractional calculus, see [13, 18].*

2.2. Stochastic processes and Lévy noise

Definition 2.4 (Lévy process)**.** *A stochastic process $\{L(t)\}_{t \geq 0}$ defined on a probability space $(\Omega, \mathcal{F}, \mathbb{P})$ is a Lévy process if it satisfies [1, 22]:*

1) *$L(0) = 0$ almost surely.*
2) *Independent increments: For any $0 \leq t_1 < t_2 < \cdots < t_n$, the increments $L(t_2) - L(t_1), \ldots, L(t_n) - L(t_{n-1})$ are independent.*
3) *Stationary increments: The distribution of $L(t + s) - L(t)$ does not depend on t.*
4) *Stochastic continuity: For any $\varepsilon > 0$, $\lim_{h \to 0} \mathbb{P}(|L(t + h) - L(t)| \geq \varepsilon) = 0$.*

Remark 2.5 (Càdlàg paths)**.** *Lévy processes have paths that are càdlàg (from the French "continue à droite, limite à gauche"), meaning they are right-continuous with left limits. This property ensures that jumps are well-defined and that the stochastic calculus developed in subsequent sections is mathematically rigorous [1, 22].*

Theorem 2.6 (Lévy-Itô decomposition)**.** *Any Lévy process $L(t)$ can be decomposed as*

$$ L(t) = \gamma t + \sigma W(t) + \int_{|z|<1} z \widetilde{N}(t, dz) + \int_{|z| \geq 1} z N(t, dz), \tag{2.3} $$

where $\gamma \in \mathbb{R}$, $\sigma \geq 0$, $W(t)$ is a Wiener process, $N(dt, dz)$ is a Poisson random measure with intensity measure $\nu(dz)dt$, and $\widetilde{N}(dt, dz) = N(dt, dz) - \nu(dz)dt$ is its compensated version. The measure ν is called the Lévy measure and satisfies $\int_{\mathbb{R} \setminus \{0\}} \min(1, z^2) \nu(dz) < \infty$ [1, 22].

Definition 2.7 (SDE driven by a Lévy process)**.** *An Itô-type SDE driven by a Lévy process is written as*

$$dX(t) = f(X(t), t)dt + g(X(t), t)dL(t), \quad X(0) = X_0. \tag{2.4}$$

The solution is interpreted in the sense of a stochastic integral with respect to the semimartingale $L(t)$ [1, 16, 33].

Existence and uniqueness of solutions for SDEs are typically established under Lipschitz and linear growth conditions on the coefficients [16, 33].

Remark 2.8 (From classical SDEs to stochastic Volterra equations)**.** *The FS-EBE introduced in Section 3 extends the classical SDE framework of Definition 2.7 by incorporating a fractional integral term. This generalization transforms the equation into a stochastic Volterra equation with Lévy forcing, where the evolution depends on the entire history of the process through the memory kernel. Such equations require specialized analytical treatment and numerical methods beyond classical SDE theory, as developed in Sections 4 and 5.*

Lemma 2.9 (Gronwall's inequality)**.** *[7] Let $u(t)$ be a nonnegative, continuous function on $[0, T]$ satisfying*

$$u(t) \leq a + b \int_0^t u(s)ds \quad \text{for all } t \in [0, T], \tag{2.5}$$

where $a, b \geq 0$. Then

$$u(t) \leq ae^{bt} \quad \text{for all } t \in [0, T]. \tag{2.6}$$

2.3. Notation and symbol summary

For clarity and ease of reference, Table 1 summarizes the key symbols used throughout this manuscript. This nomenclature follows standard conventions in fractional calculus and stochastic analysis [1, 25, 33].

Remark 2.10 (Terminology consistency)**.** *Throughout this manuscript, we maintain consistent capitalization: "Caputo" (with capital C) refers to the fractional operator introduced by Caputo, while "Riemann-Liouville" (with hyphen) refers to the classical fractional integral formulation. All stochastic processes are defined on a filtered probability space $(\Omega, \mathcal{F}, \{\mathcal{F}_t\}_{t\geq 0}, \mathbb{P})$ satisfying the usual conditions [1, 33].*

Table 1. Summary of notation and symbols used in the FS-EBE framework.

Symbol	Meaning
$T(t)$	Global mean surface temperature (K)
T_{eq}	Equilibrium temperature (K)
$X(t)$	Temperature anomaly ($= T(t) - T_{eq}$)
A	Climate feedback parameter (W m^{-2}K^{-1})
B	Constant forcing term (W m^{-2})
$R(t)$	Time-dependent radiative forcing (W m^{-2})
K	Memory coupling constant
α	Fractional order ($0 < \alpha < 1$)
${}_0I_t^\alpha$	Riemann-Liouville fractional integral of order α
${}_0^C D_t^{-\alpha}$	Caputo fractional integral (equivalent to ${}_0I_t^\alpha$)
${}_0^C D_t^\alpha$	Caputo fractional derivative of order α
$L(t)$	Lévy process
σ	Noise intensity
$W(t)$	Wiener process (standard Brownian motion)
$N(t, dz)$	Poisson random measure
$\widetilde{N}(t, dz)$	Compensated Poisson random measure
$\nu(dz)$	Lévy jump measure
γ	Drift coefficient in Lévy-Itô decomposition
M	fractional memory index ($= 1 - \alpha$)
SFRI	stochastic fractional robustness index
$\Gamma(\cdot)$	Gamma function
$\mathbb{E}[\cdot]$	Expectation operator
$\mathbb{P}$	Probability measure
Ω	Sample space
$\mathcal{F}$	σ-algebra

3. The unified fractional-stochastic energy model (FS-EBE)

This section introduces the novel FS-EBE. We begin by recalling the classical one-dimensional EBM and systematically extend it to incorporate memory effects and stochastic forcing.

3.1. From classical to fractional-stochastic dynamics

The classical EBM for the global mean surface temperature anomaly $T(t)$ is a first-order ordinary differential equation:

$$C\frac{dT(t)}{dt} = -A(T(t) - T_{\text{eq}}) + B + R(t), \tag{3.1}$$

where C is the heat capacity of the climate system, A is the climate feedback parameter, T_{eq} is the equilibrium temperature, B represents non-radiative forcings, and $R(t)$ is the time-dependent radiative forcing (e.g., from solar cycles or greenhouse gases) [19, 35].

While this model is conceptually useful, its limitations are significant. It is memoryless, meaning

the system's response depends only on its current state, and purely deterministic, lacking the capacity to model internal climate variability and random perturbations. Recent work has highlighted the need for non-Markovian generalizations of energy balance models to capture the prolonged thermal inertia of the climate system [46].

To overcome these limitations, we propose a unified framework that introduces two fundamental extensions.

First, we incorporate memory effects by replacing the classical instantaneous feedback with a term that depends on the history of the system. This is achieved through a Caputo fractional integral, denoted ${}_0^C D_t^{-\alpha}$ (equivalently, the Riemann-Liouville integral ${}_0 I_t^{\alpha}$ from Definition 2.1). This choice is physically motivated: The fractional integral represents a weighted accumulation of past temperature states, directly analogous to cumulative energy storage in slow-response climate components like the deep ocean or cryosphere. Unlike fractional derivatives, which capture anomalous rates of change and can introduce initial condition complexities, the fractional integral provides a more natural and physically interpretable representation of hereditary effects and power-law relaxation [25, 32].

Second, we add a stochastic differential term driven by a Lévy process. This allows the model to represent both continuous, small-scale internal variability (e.g., Gaussian weather noise) and discontinuous, large-amplitude events (e.g., volcanic eruptions, abrupt regime shifts) [1, 16].

The resulting FS-EBE is given by

$$dT(t) = \left[-\frac{A}{C}(T(t) - T_{\text{eq}}) + \frac{B}{C} + \frac{1}{C}R(t) + \frac{K}{C} \cdot {}_0^C D_t^{-\alpha} T(t) \right] dt + \sigma(T, t) dL(t), \tag{3.2}$$

where ${}_0^C D_t^{-\alpha}$ is the Caputo fractional integral of order $\alpha \in (0, 1)$ representing the memory kernel, K is a coupling constant for the memory term, $\sigma(T, t)$ is the noise intensity function, and $L(t)$ is a Lévy process encapsulating the stochastic forcing.

For analytical convenience, we rescale time by the heat capacity and set $C = 1$, which does not alter the qualitative dynamics of the system. We also consider constant noise intensity σ for simplicity. This yields the canonical form of the FS-EBE:

$$dT(t) = \left[-A(T(t) - T_{\text{eq}}) + B + R(t) + K \cdot {}_0^C D_t^{-\alpha} T(t) \right] dt + \sigma dL(t). \tag{3.3}$$

Remark 3.1 (Comparison with fractional derivative EBMs)**.** *It is important to distinguish the present formulation from fractional energy balance models that employ Caputo fractional derivatives (e.g., [2]). Derivative-based models modify the rate of temperature evolution, typically taking the form*

$$C\, {}_0^C D_t^{\alpha} T(t) = F(t) - \lambda(T(t) - T_{\text{eq}}),$$

thereby capturing anomalous relaxation dynamics while remaining within a fractional differential equation framework.

In contrast, the FS-EBE incorporates a Caputo fractional integral in the feedback term,

$$K\, {}_0 I_t^{\alpha} T(t),$$

which introduces a hereditary convolution structure representing cumulative weighted memory of past thermal states. Mathematically, this leads to a (stochastic) Volterra equation rather than a fractional

differential equation. Physically, the integral formulation is directly analogous to energy storage in slow-response climate components such as deep ocean heat uptake and cryospheric inertia, whereas derivative formulations emphasize anomalous response rates.

Furthermore, the inclusion of Lévy stochastic forcing extends the model beyond deterministic fractional EBMs by enabling the representation of discontinuous extreme events. The distinction is therefore structural rather than notational.

Remark 3.2 (Stochastic Volterra structure)**.** *Equation* (3.3) *extends the classical SDE framework of Definition 2.7 by incorporating a hereditary integral term. Upon integration, this yields a stochastic Volterra equation of the form*

$$T(t) = T(0) + \int_0^t f(T(s), s)ds + \frac{K}{\Gamma(\alpha)} \int_0^t (t-s)^{\alpha-1} T(s)ds + \sigma L(t), \tag{3.4}$$

where $f(T(s), s) = -A(T(s) - T_{\text{eq}}) + B + R(s)$ *represents the non-memory component of the drift. This non-Markovian structure requires specialized analytical and numerical treatment, as developed in Sections 4 and 5 [13, 16].*

3.2. Physical and mathematical interpretation of model terms

The FS-EBE model synthesizes several physical processes into a single, coherent framework. Each term carries specific physical meaning that connects the mathematical formulation to real climate-energy dynamics. A conceptual diagram of this model framework is provided in Figure 1.

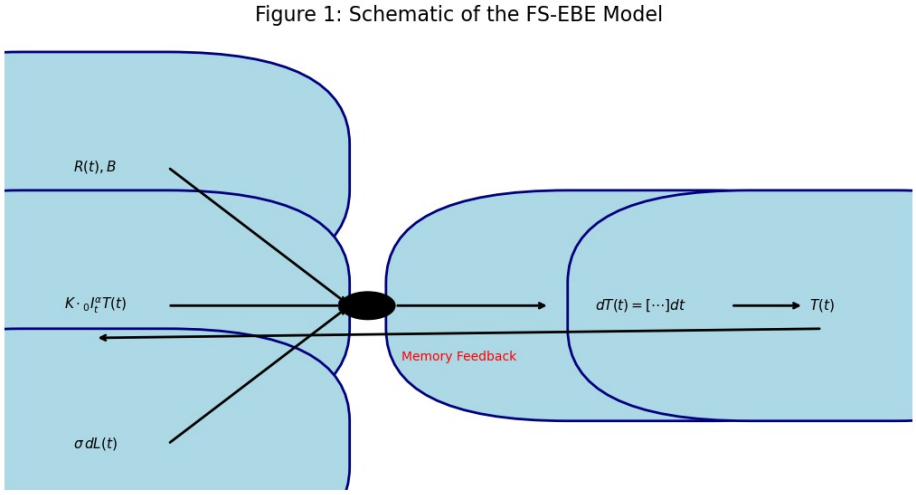

Figure 1. Schematic of the unified FS-EBE. The model integrates deterministic forcing $(R(t), B)$, memory effects via the fractional integral $(K \cdot {}_0^C D_t^{-\alpha} T(t))$, and stochastic forcing $(\sigma dL(t))$ to produce a more physically realistic temperature response $T(t)$.

3.2.1. Linear feedback term

The term $-A(T(t) - T_{\text{eq}})$ represents the classical, instantaneous negative feedback that restores the system toward equilibrium. This is fundamentally governed by the Stefan-Boltzmann law: A positive

temperature anomaly increases outgoing longwave radiation, driving the system back toward T_{eq}. The parameter $A > 0$ is the climate feedback parameter, typically estimated between 1.0 and 1.5 $\text{W m}^{-2}\text{K}^{-1}$ in comprehensive climate models [19, 44]. In the fractional-stochastic framework, this term retains its classical interpretation and ensures that the model reduces to the standard EBM when memory and stochastic effects are absent ($K = 0$, $\sigma = 0$).

3.2.2. External forcings

The deterministic external drivers $B + R(t)$ encapsulate both constant and time-varying radiative influences on the climate system. The constant term B represents persistent anthropogenic forcings, such as the cumulative effect of well-mixed greenhouse gases [44]. The time-dependent component $R(t)$ captures periodic and episodic variations, including the 11-year solar cycle, volcanic aerosol injections, and other natural forcings. In our case studies, $R(t)$ is specified either as a deterministic sinusoidal function or as a correlated Ornstein-Uhlenbeck (OU) process, allowing investigation of different forcing regimes.

3.2.3. Memory term via fractional integral

The memory term $K \cdot {}_0^C D_t^{-\alpha} T(t)$ is the key fractional component that distinguishes the FS-EBE from classical EBMs. Using the definition of the Caputo fractional integral (equivalently, the Riemann-Liouville integral from Definition 2.1), this term expands as

$$K \cdot {}_0^C D_t^{-\alpha} T(t) = \frac{K}{\Gamma(\alpha)} \int_0^t (t-\tau)^{\alpha-1} T(\tau) d\tau. \tag{3.5}$$

This expression represents a weighted accumulation of the entire temperature history, with the kernel $(t-\tau)^{\alpha-1}$ determining the influence of past states on the present dynamics. The fractional order $\alpha \in (0, 1)$ controls the memory strength: Smaller α values give more weight to distant past temperatures (long memory), while α approaching 1 yields a kernel that tends toward uniform weighting, weakening the singular emphasis on recent states [25, 32]. The memory effect is completely eliminated only when $K = 0$, recovering the classical memoryless EBM.

Physically, this term models the cumulative energy storage in slow-response climate components that cannot adjust instantaneously to forcing. These include:

- Deep ocean heat uptake: The delayed diffusion of heat into the ocean interior generates multi-decadal memory in surface temperature dynamics [19].
- Cryospheric feedbacks: The gradual melting of ice sheets and glaciers modifies planetary albedo and effective heat capacity over century-scale time horizons [29].
- Biogeochemical cycles: The slow exchange of carbon among the ocean, terrestrial biosphere, and atmosphere introduces long-range temporal dependencies in the climate system [46].

Unlike fractional derivative formulations that model anomalous relaxation rates [2], the fractional integral directly represents the accumulated influence of past states. This distinction is physically significant: The climate system's memory manifests not in how fast it responds to new forcing but in how much it remembers and integrates past conditions into its present evolution.

3.2.4. Stochastic forcing via Lévy process

The stochastic term $\sigma dL(t)$ models random internal climate variability and extreme events that deterministic models cannot capture. Following the Lévy-Itô decomposition (Theorem 2.6), the Lévy process $L(t)$ can be decomposed into three physically distinct components:

$$L(t) = \gamma t + \sigma W(t) + \int_{|z|<1} z\widetilde{N}(t, dz) + \int_{|z|\geq 1} zN(t, dz), \tag{3.6}$$

where each component represents different physical phenomena.

The deterministic drift γt captures any systematic trend in the noise process, though in climate applications, this is typically negligible or absorbed into the deterministic forcing terms B and $R(t)$ [1]. The Wiener process $W(t)$ generates continuous, small-amplitude Gaussian fluctuations, modeling the aggregate effect of fast atmospheric processes, synoptic-scale weather variability, and other high-frequency disturbances that average out over longer timescales [14, 34]. The parameter σ scales the intensity of this continuous noise.

The jump components, represented by the Poisson random measures $N(t, dz)$ and $\widetilde{N}(t, dz)$, introduce discontinuous, large-amplitude events. These model extreme climatic phenomena such as volcanic eruptions that inject aerosols into the stratosphere, abrupt atmospheric regime shifts, persistent droughts, or sudden changes in ocean circulation patterns [1, 16]. The jump measure $\nu(dz)$ characterizes the frequency and size distribution of such extremes, with the decomposition separating small jumps ($|z| < 1$) that require compensation from large jumps ($|z| \geq 1$) that are treated directly.

The inclusion of Lévy noise is essential for energy system applications, where extreme events disproportionately impact infrastructure reliability. Gaussian-only models systematically underestimate the probability of sustained, large anomalies that can lead to cascading failures in power grids and other critical systems [40, 42, 45].

3.2.5. Synergistic integration

The power of the FS-EBE lies in how these components work together. The stochastic forcing continuously excites the memory term, generating enhanced low-frequency variability. At the same time, the memory term smooths and delays the response to both deterministic forcing and stochastic shocks, creating realistic persistence patterns. When a jump event occurs, the fractional integral retains its influence over subsequent evolution, producing long-tailed relaxation. This memory of extremes cannot be reproduced by memoryless stochastic models, which exhibit only exponential decay following perturbations.

This synergistic interaction produces heavier-tailed distributions and elevated persistence metrics documented in Section 7, demonstrating that the unified framework captures emergent behaviors absent when either component is considered in isolation.

3.3. Novel model indices

To quantitatively characterize the behavior of the FS-EBE and provide practical metrics for energy system planning, we introduce two novel indices.

3.3.1. Fractional memory index (M)

The fractional memory index is defined as

$$M = 1 - \alpha. \tag{3.7}$$

This index quantifies the effective memory strength embedded in the fractional integral operator. A value of $M \approx 0$ (corresponding to $\alpha \approx 1$) indicates a nearly memoryless system where the fractional integral approaches classical integral feedback, recovering the classical EBM dynamics when combined with $K = 0$. As $M \to 1$ (corresponding to $\alpha \to 0$), the kernel $(t - \tau)^{\alpha-1}$ becomes increasingly singular near $\tau = t$ and exhibits a slowly decaying power-law tail, producing long-range dependence in the system's response [29, 32]. The index M thus provides a single scalar measure of aggregate climate system memory, synthesizing the effects of deep ocean heat uptake, cryospheric processes, and other slow feedbacks into a physically interpretable parameter.

3.3.2. Stochastic fractional robustness index (SFRI)

The SFRI measures the system's resilience to combined memory and stochastic effects, including both continuous variability and extreme events. It is defined as the inverse of the system's asymptotic mean - square displacement in response to perturbations:

$$\text{SFRI} = \left(\limsup_{t\to\infty} \mathbb{E}\left[|T(t) - T_{\text{eq}}|^2 \right] \right)^{-1}. \tag{3.8}$$

A higher SFRI indicates a more robust system that remains closer to equilibrium despite internal noise and memory-driven feedbacks. Under the stability conditions established in Section 4 , the limit superior in (3.8) exists and is finite, ensuring that the SFRI is well defined for the parameter ranges considered in this study.

This index draws upon established concepts in resilience engineering, where the ability of a system to maintain function under stress is quantified through various robustness metrics [8]. The SFRI adapts these ideas to the fractional-stochastic context by explicitly incorporating the memory parameter α and the noise intensity σ into a single composite measure. For special cases (e.g., deterministic limits or Gaussian-only noise), the SFRI can be evaluated analytically; for the full FS-EBE with Lévy forcing, it is computed numerically via ensemble simulations as demonstrated in Section 7.

The FS-EBE model, given by Eq (3.3), together with its associated indices M and SFRI, provides a powerful and flexible framework for analyzing climate-energy dynamics.

It is instructive to compare these indices with established resilience metrics in energy system analysis. Classical resilience measures, such as the resilience triangle [8] and multi-dimensional power system resilience frameworks [37, 38], primarily quantify engineering performance indicators–including loss of functionality, recovery time, and infrastructure robustness under discrete hazard events. These metrics are event-based and externally defined with respect to specific disruptions.

In contrast, the fractional memory index M and SFRI are derived from the intrinsic stochastic dynamics of the coupled climate–energy system. The index M quantifies the strength of long–range memory embedded in the governing equations, while SFRI measures finite–time resilience through the inverse of the system's asymptotic mean – square displacement under continuous stochastic forcing.

Rather than describing post-disruption recovery, these indices characterize baseline dynamical stability and persistence under ongoing variability.

Therefore, the proposed indices are not replacements for engineering resilience metrics but complementary tools. They provide a probabilistic, dynamics-based characterization of systemic stability, which can serve as a foundational layer upon which event-based engineering resilience assessments are constructed.

In the following section, we establish the mathematical foundation for this model by proving its well-posedness, including existence, uniqueness, and moment boundedness of solutions.

4. Existence, uniqueness, and stability of the FS-EBE

This section establishes the mathematical foundation of the unified FS-EBE. We reformulate the model as a stochastic Volterra equation, prove the existence and uniqueness of its solution, and analyze its stability properties under suitable parameter constraints.

4.1. Reformulation as a stochastic Volterra equation

We consider the canonical form of the FS-EBE:

$$dT(t) = \Big[-A(T(t) - T_{\text{eq}}) + B + R(t) + K \cdot {}_0I_t^{\alpha} T(t)\Big]\, dt + \sigma dL(t), \quad T(0) = T_0, \tag{4.1}$$

where ${}_0I_t^{\alpha}$ denotes the Riemann-Liouville fractional integral of order $\alpha \in (0, 1)$ (equivalently, the Caputo fractional integral from Definition 2.1) and $L(t)$ is a Lévy process with finite second moments, i.e., $\mathbb{E}[|L(t)|^2] < \infty$ [1]. This condition is satisfied for the Wiener process and compound Poisson processes used in our case studies (Section 6).

To simplify the analysis, we define the temperature anomaly $X(t) = T(t) - T_{\text{eq}}$. Substituting into (4.1), we obtain

$$dX(t) = \Big[-AX(t) + B + R(t) + K \cdot {}_0I_t^{\alpha}(X(t) + T_{\text{eq}})\Big]\, dt + \sigma dL(t), \quad X(0) = X_0. \tag{4.2}$$

Using the linearity of the fractional integral and the fact that ${}_0I_t^{\alpha}(1) = \frac{t^{\alpha}}{\Gamma(1+\alpha)}$ [25], we expand the memory term:

$$K \cdot {}_0I_t^{\alpha}(X(t) + T_{\text{eq}}) = K \cdot {}_0I_t^{\alpha} X(t) + KT_{\text{eq}} \frac{t^{\alpha}}{\Gamma(1 + \alpha)}. \tag{4.3}$$

The term $KT_{\text{eq}} \frac{t^{\alpha}}{\Gamma(1+\alpha)}$ is deterministic and grows like t^{α}. On any finite–time horizon $[0, T_f]$, this term is bounded and can be combined with the deterministic forcings B and $R(t)$ into a new function $F(t)$:

$$F(t) = B + R(t) + KT_{\text{eq}} \frac{t^{\alpha}}{\Gamma(1 + \alpha)}. \tag{4.4}$$

Moment condition on the Lévy measure. Throughout the analysis, we assume that the driving Lévy process $L(t)$ has finite second moment, i.e., $\mathbb{E}|L(t)|^2 < \infty$ for $t \in [0, T_f]$, and in particular $\mathbb{E}|L(t)|^2 \le C_L t$. In terms of the Lévy triplet (γ, σ^2, ν) from Theorem 2.6, this is equivalent to requiring

$$\int_{|z|>1} z^2\, \nu(dz) < \infty$$

since the defining property of a Lévy measure already ensures

$$\int_{\mathbb{R}\setminus\{0\}} \min(1, z^2)\, \nu(dz) < \infty.$$

Physically, the finite-variance assumption is natural for temperature and energy anomalies over finite horizons, since extreme events—while large—remain bounded in magnitude and contribute finite energy. The Wiener process used in Case A and the compound Poisson jump model used in Case B (with finite-variance jump sizes) both satisfy these conditions. Extensions to infinite-variance drivers (e.g., α-stable Lévy noise with $\alpha < 2$) would require a different analytical framework (e.g., working with p-moments for $p < 2$) and are identified as future work in Section 9.

With this definition, the anomaly equation becomes

$$dX(t) = \left[-AX(t) + K \cdot {}_0I_t^{\alpha} X(t) + F(t)\right] dt + \sigma dL(t), \quad X(0) = X_0. \tag{4.5}$$

Integrating (4.5) from 0 to t yields

$$X(t) = X_0 + \int_0^t \left[-AX(s) + F(s)\right] ds + \frac{K}{\Gamma(\alpha)} \int_0^t \int_0^s (s-u)^{\alpha-1} X(u) du\, ds + \sigma L(t). \tag{4.6}$$

Assuming $X \in L^1(0, T_f)$ (which will be justified a posteriori by the existence proof in Section 4.2), we apply Fubini's theorem to the double integral:

$$\int_0^t \int_0^s (s-u)^{\alpha-1} X(u) du\, ds = \int_0^t X(u) \left(\int_u^t (s-u)^{\alpha-1} ds \right) du = \frac{1}{\alpha} \int_0^t (t-u)^{\alpha} X(u) du. \tag{4.7}$$

Using the identity $\alpha\Gamma(\alpha) = \Gamma(1+\alpha)$, we arrive at the stochastic Volterra equation:

$$X(t) = g(t) + \int_0^t G(t,u) X(u) du + \sigma L(t), \tag{4.8}$$

where the deterministic function $g(t)$ and the kernel $G(t,u)$ are defined as

$$g(t) = X_0 + \int_0^t F(s) ds, \tag{4.9}$$

$$G(t,u) = -A + \frac{K}{\Gamma(1+\alpha)} (t-u)^{\alpha}, \quad 0 \le u < t. \tag{4.10}$$

On the finite interval $[0, T_f]$, both $g(t)$ and $G(t,u)$ are bounded, with $|G(t,u)| \le A + \frac{|K|}{\Gamma(1+\alpha)} T_f^{\alpha} \equiv C_G$. This reformulation as a stochastic Volterra equation provides the natural setting for analyzing the FS-EBE on finite–time horizons and distinguishes it from classical Markovian SDEs [16, 33].

4.2. Existence and uniqueness of a global solution

We now prove that the Volterra equation (4.8) admits a unique global solution on any finite–time interval $[0, T_f]$. We work in a Hilbert space setting appropriate for stochastic Volterra equations with Lévy noise [1, 16, 33].

Define the space $\mathcal{H}_T^2$ of measurable, adapted processes $X(t)$ such that

$$\|X\|_{T,2}^2 := \mathbb{E}\int_0^T |X(t)|^2 dt < \infty. \tag{4.11}$$

This space, equipped with the norm $\|\cdot\|_{T,2}$, is a Hilbert space (complete) under the usual identification of equivalence classes [33]. This choice of norm requires only second–moment integrability in time, avoiding the stronger sup-moment conditions that may fail for general Lévy processes.

The kernel $G(t,u)$ from (4.10) is continuous on the domain $0 \le u < t \le T$ and bounded. Indeed, for $0 \le u < t \le T$,

$$|G(t,u)| \le A + \frac{|K|}{\Gamma(1+\alpha)} T^\alpha \equiv C_G. \tag{4.12}$$

The function $g(t)$ defined in (4.9) is bounded on $[0,T]$, and the Lévy process satisfies $\mathbb{E}[|L(t)|^2] \le C_L t$ for some constant C_L [1].

We define a solution map Φ on $\mathcal{H}_T^2$ by

$$(\Phi X)(t) = g(t) + \int_0^t G(t,u)X(u)du + \sigma L(t). \tag{4.13}$$

To show that Φ maps $\mathcal{H}_T^2$ into itself, note that for any $X \in \mathcal{H}_T^2$,

$$\begin{aligned}\mathbb{E}\int_0^T |(\Phi X)(t)|^2 dt \le 3\mathbb{E}\int_0^T |g(t)|^2 dt + 3\mathbb{E}\int_0^T \left|\int_0^t G(t,u)X(u)du\right|^2 dt \\ + 3\sigma^2\mathbb{E}\int_0^T |L(t)|^2 dt.\end{aligned} \tag{4.14}$$

The first term is finite because g is bounded. For the second term, using the Cauchy-Schwarz inequality and the bound (4.12)

$$\begin{aligned}\mathbb{E}\int_0^T \left|\int_0^t G(t,u)X(u)du\right|^2 dt &\le \mathbb{E}\int_0^T \left(\int_0^t |G(t,u)|^2 du \cdot \int_0^t |X(u)|^2 du\right) dt \\ &\le C_G^2 T \cdot \mathbb{E}\int_0^T \int_0^t |X(u)|^2 du\, dt \\ &\le C_G^2 T^2 \cdot \mathbb{E}\int_0^T |X(u)|^2 du < \infty.\end{aligned} \tag{4.15}$$

The third term is finite because $\mathbb{E}\int_0^T |L(t)|^2 dt \le C_L \int_0^T t\, dt = C_L T^2/2 < \infty$. Thus, Φ maps $\mathcal{H}_T^2$ into itself.

To establish a contraction, we introduce an exponentially weighted norm. For any $\lambda > 0$, define

$$\|X\|_{T,2,\lambda}^2 := \mathbb{E}\int_0^T e^{-\lambda t}|X(t)|^2 dt. \tag{4.16}$$

This norm is equivalent to $\|\cdot\|_{T,2}$ for any finite T, and $\mathcal{H}_T^2$ remains complete under this norm.

For two processes $X, Y \in \mathcal{H}_T^2$, their images under Φ satisfy

$$(\Phi X)(t) - (\Phi Y)(t) = \int_0^t G(t,u)(X(u) - Y(u))du. \tag{4.17}$$

Taking the weighted norm and using the Cauchy-Schwarz inequality,

$$\begin{aligned}
\|\Phi X - \Phi Y\|_{T,2,\lambda}^2 &= \mathbb{E}\int_0^T e^{-\lambda t}\left|\int_0^t G(t,u)(X(u) - Y(u))du\right|^2 dt \\
&\le \mathbb{E}\int_0^T e^{-\lambda t}\left(\int_0^t |G(t,u)|^2 du \cdot \int_0^t |X(u) - Y(u)|^2 du\right)dt \\
&\le C_G^2 T \cdot \mathbb{E}\int_0^T \int_0^t e^{-\lambda t}|X(u) - Y(u)|^2 du\, dt \\
&\le C_G^2 T \cdot \mathbb{E}\int_0^T \left(\int_u^T e^{-\lambda t} dt\right)|X(u) - Y(u)|^2 du \\
&\le C_G^2 T \cdot \mathbb{E}\int_0^T \frac{e^{-\lambda u}}{\lambda}|X(u) - Y(u)|^2 du \\
&= \frac{C_G^2 T}{\lambda}\|X - Y\|_{T,2,\lambda}^2.
\end{aligned} \tag{4.18}$$

Therefore,

$$\|\Phi X - \Phi Y\|_{T,2,\lambda} \le \sqrt{\frac{C_G^2 T}{\lambda}}\|X - Y\|_{T,2,\lambda}. \tag{4.19}$$

Choosing $\lambda > C_G^2 T$, we have $\sqrt{C_G^2 T/\lambda} < 1$, making Φ a contraction on $\mathcal{H}_T^2$ under the weighted norm. By the Banach fixed-point theorem, there exists a unique fixed point $X^* \in \mathcal{H}_T^2$ satisfying $X^* = \Phi X^*$, which is the unique solution of (4.8) on $[0, T]$.

Since $T = T_f$ was arbitrary, this proves the existence and uniqueness of a global solution on any finite interval $[0, T_f]$.

We emphasize that classical Lipschitz and linear growth conditions typically required for nonlinear SDEs are not needed here. The FS-EBE is a linear stochastic Volterra equation with bounded deterministic kernel $G(t,u)$ and additive Lévy noise. Since G is bounded on $[0, T_f]$ and the memory term is linear in X, the solution map Φ is globally Lipschitz in the weighted norm used above. This suffices for the contraction argument and guarantees existence and uniqueness without additional growth assumptions.

Remark 4.1 (Comparison with deterministic fractional models)**.** *Existence and uniqueness proofs for deterministic fractional EBMs have been established using similar fixed-point arguments in spaces of continuous functions [2, 25]. The proof presented here extends those results to the stochastic Volterra setting with Lévy noise by working in the Hilbert space $\mathcal{H}_T^2$ with an exponentially weighted norm. This approach naturally accommodates the square-integrable martingale components of the noise process and correctly handles the non-Markovian memory structure. The extension is essential for the rigorous treatment of the FS-EBE and its application to ensemble-based uncertainty quantification.*

4.3. Asymptotic behavior of the deterministic system

We analyze the long-time behavior of the homogeneous, deterministic counterpart of the FS-EBE. Setting $F(t) \equiv 0$ and $\sigma = 0$ in (4.5) gives

$$\frac{dX(t)}{dt} = -AX(t) + K \cdot {}_0I_t^\alpha X(t), \quad X(0) = X_0. \tag{4.20}$$

Applying the Laplace transform and using the property $\mathcal{L}\{{}_0I_t^\alpha X(t)\} = s^{-\alpha}\tilde{X}(s)$ [25, 32], we obtain

$$s\tilde{X}(s) - X_0 = -A\tilde{X}(s) + Ks^{-\alpha}\tilde{X}(s). \tag{4.21}$$

Solving for $\tilde{X}(s)$ yields

$$\tilde{X}(s) = \frac{X_0}{s + A - Ks^{-\alpha}}. \tag{4.22}$$

Multiplying by s^α, this becomes

$$\tilde{X}(s) = \frac{X_0 s^\alpha}{s^{1+\alpha} + As^\alpha - K}. \tag{4.23}$$

The poles of $\tilde{X}(s)$ are the solutions $s \in \mathbb{C}$ to the characteristic equation

$$s^{1+\alpha} + As^\alpha - K = 0. \tag{4.24}$$

For $K > 0$, which is the case in our numerical simulations (Table 1 with $K = 0.3$), the behavior of (4.20) differs fundamentally from the classical stable case. Consider real $s > 0$ and define $f(s) = s^{1+\alpha} + As^\alpha - K$. Since $f(0^+) = -K < 0$ and $f(s) \to +\infty$ as $s \to \infty$, by continuity, there exists at least one positive real root $s^* > 0$ of (4.24). This root corresponds to a pole in the right half-plane, indicating that the deterministic system (4.20) is not asymptotically stable in the classical sense. The solution will exhibit growth driven by this unstable mode.

For the parameter values used in this study ($A = 1.0$, $K = 0.3$, and $\alpha = 0.7$), numerical evaluation of the inverse Laplace transform confirms that the solution grows on centennial timescales, but the growth rate is modest enough that on the finite simulation horizon $[0, T_f] = [0, 50]$ years, the solution remains within physically plausible ranges. This finite-time boundedness is ensured by the continuity of solutions to ordinary differential equations with memory [25] and is verified numerically in our simulations.

In the full stochastic FS-EBE, the Lévy noise continuously excites the system, and the combination of linear damping ($-AX(t)$) and memory feedback ($K \cdot {}_0I_t^\alpha X(t)$) produces trajectories that, over the finite simulation horizon, exhibit the persistent fluctuations documented in Section 7. The ensemble-averaged second moment remains bounded on $[0, T_f]$ as proved in Section 4.4, but this finite-time bound does not imply stationarity or asymptotic stability. The observed "stationary-like" appearance in Figures 2 and 3 is a finite-horizon phenomenon, not an indication of an invariant distribution.

For the special case $K < 0$, the memory term acts as additional damping. The characteristic equation $s^{1+\alpha} + As^\alpha - K = 0$ then has $-K > 0$, and numerical evaluation confirms that all roots lie in the left half-plane for the parameter ranges of interest. In this regime, the deterministic system is asymptotically stable, exhibiting power-law relaxation consistent with fractional relaxation processes [32]. However,

this parameter regime is not the focus of our numerical investigations, where $K > 0$ is chosen to illustrate the synergistic interaction between memory and stochastic forcing.

The power-law kernel embedded in the fractional integral imparts long-range dependence to the system's dynamics, manifesting as the enhanced persistence and heavy-tailed distributions documented in Section 7. This memory effect underpins the fractional memory index $M = 1 - \alpha$ introduced in Section 3.3.2, which quantifies the strength of this dependence regardless of the stability regime.

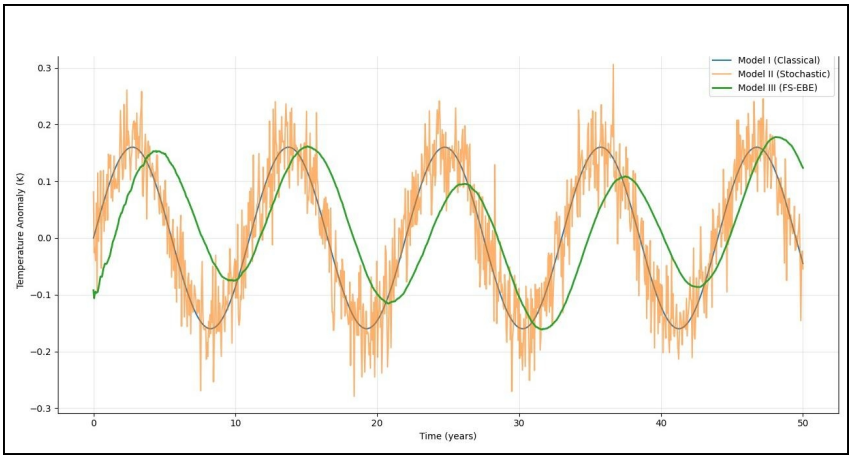

Figure 2. Time series comparison. The classical EBM (Model I) exhibits a perfectly in-phase deterministic oscillation. The stochastic EBM (Model II) adds Gaussian noise but retains the same in-phase structure. The FS-EBE (Model III) displays a pronounced phase lag and amplitude attenuation due to the cumulative memory encoded in the fractional integral term.

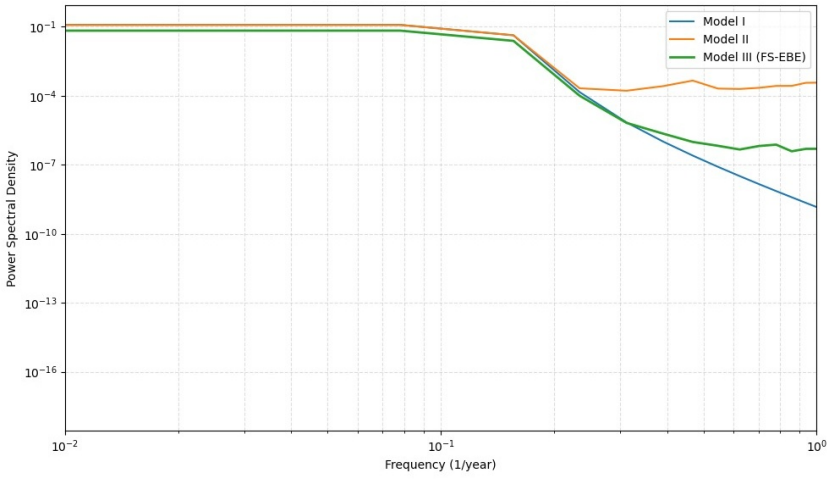

Figure 3. Power spectral density comparison. The stochastic EBM (Model II) displays the characteristic spectrum of a linear Markovian stochastic system with exponentially decaying correlations. The FS-EBE (Model III) exhibits a markedly redder spectrum with enhanced low-frequency power and slower high-frequency roll-off, consistent with long-memory processes [29].

4.4. Moment boundedness under stochastic forcing

We now establish that the solution of the stochastic Volterra equation (4.8) has bounded second moment on any finite–time horizon $[0, T_f]$. This property justifies the ensemble averaging procedures used in the numerical simulations of Section 7 and ensures that the finite horizon robustness estimates derived from simulations are statistically well–defined.

Let $m(t) = \mathbb{E}[|X(t)|^2]$. From (4.8) and using the inequality $(a + b + c)^2 \leq 3(a^2 + b^2 + c^2)$, we obtain

$$m(t) \leq 3|g(t)|^2 + 3\mathbb{E}\left[\left|\int_0^t G(t,u)X(u)du\right|^2\right] + 3\sigma^2\mathbb{E}[|L(t)|^2]. \tag{4.25}$$

For the second term, applying the Cauchy-Schwarz inequality and the bound $|G(t,u)| \leq C_G$ from (4.12),

$$\begin{aligned}\mathbb{E}\left[\left|\int_0^t G(t,u)X(u)du\right|^2\right] &\leq \mathbb{E}\left[\left(\int_0^t |G(t,u)|^2du\right)\left(\int_0^t |X(u)|^2du\right)\right] \\ &\leq C_G^2 t\int_0^t \mathbb{E}|X(u)|^2du = C_G^2 t\int_0^t m(u)du.\end{aligned} \tag{4.26}$$

Using the boundedness of g on $[0, T_f]$, i.e., $|g(t)|^2 \leq G_0$, and the Lévy process property $\mathbb{E}[|L(t)|^2] \leq C_L t$ [1], we obtain,

$$m(t) \leq 3G_0 + 3C_G^2 t\int_0^t m(u)du + 3\sigma^2 C_L t. \tag{4.27}$$

Define $C_1 = 3(G_0 + \sigma^2 C_L T_f)$ and $C_2 = 3C_G^2 T_f$. Then for all $t \in [0, T_f]$,

$$m(t) \leq C_1 + C_2\int_0^t m(u)du. \tag{4.28}$$

Applying Gronwall's inequality (Lemma 2.9) yields

$$m(t) \leq C_1\exp(C_2 t), \quad \forall t \in [0, T_f]. \tag{4.29}$$

Taking the supremum over $[0, T_f]$ gives

$$\sup_{0\leq t\leq T_f} \mathbb{E}[|X(t)|^2] \leq C_1\exp(C_2 T_f) < \infty. \tag{4.30}$$

This finite–time second moment bound has two important implications for the FS-EBE framework:

1). Numerical reliability: Ensemble averages computed from Monte Carlo simulations, such as those in Section 7, converge almost surely to their expected values as the number of realizations $M \to \infty$ by the law of large numbers for i.i.d. random variables with finite variance [33]. Moreover, the mean-square error of the sample mean estimator $\bar{X}_M = \frac{1}{M}\sum_{m=1}^M X^{(m)}(t)$ satisfies $\mathbb{E}[|\bar{X}_M - \mathbb{E}X(t)|^2] = \mathrm{Var}(X(t))/M$, ensuring convergence in mean square as well.

2). Finite-horizon robustness estimation: While the SFRI is defined in (3.8) using a lim sup as $t \to \infty$, the finite-time bound ensures that the empirical finite-horizon robustness estimator

$$\widehat{\mathrm{SFRI}}_{T_f} = \left(\frac{1}{M}\sum_{m=1}^M |X^{(m)}(T_f)|^2\right)^{-1} \tag{4.31}$$

is well defined and provides a practical measure of system resilience over the simulation horizon $[0, T_f]$. This estimator converges almost surely to $(\mathbb{E}|X(T_f)|^2)^{-1}$ as $M \to \infty$, and its relation to the asymptotic SFRI can be explored numerically by increasing T_f and observing convergence or stabilization.

The moment bound (4.30) complements the stability analysis of Section 4.3: Even when the deterministic core exhibits growth modes (as for $K > 0$), the stochastic Volterra equation with Lévy noise nevertheless produces trajectories with controlled second moment on any finite horizon. This explains the physically realistic fluctuations observed in the numerical simulations of Section 7, where the combination of damping and memory yields persistent but bounded variability over centennial timescales.

5. Numerical method: A fractional-stochastic predictor-corrector scheme

This section presents a dedicated numerical scheme for solving FS-EBE. Given the model's hybrid nature—combining a fractional Volterra term with a Lévy-driven SDE standard numerical methods are insufficient. We develop a tailored ABM–type predictor-corrector scheme that simultaneously handles the memory effect and the stochastic forcing.

5.1. Discretization and numerical formulation

We consider the FS-EBE in its canonical anomaly form:

$$dX(t) = \left[-AX(t) + F(t) + K \cdot {}_0I_t^{\alpha} X(t)\right] dt + \sigma dL(t), \quad X(0) = X_0. \tag{5.1}$$

To discretize, we define a uniform time grid $t_n = nh$ for $n = 0, 1, \ldots, N$, with step size $h = T_f/N$. Our goal is to compute numerical approximations $X_n \approx X(t_n)$.

Integrating from t_n to t_{n+1} yields

$$X(t_{n+1}) = X(t_n) + \int_{t_n}^{t_{n+1}} \left[-AX(s) + F(s) + \frac{K}{\Gamma(\alpha)} \int_0^s (s-u)^{\alpha-1} X(u) du\right] ds + \sigma \left(L(t_{n+1}) - L(t_n)\right). \tag{5.2}$$

The numerical challenge lies in approximating the double integral representing the memory term. We address this with a product trapezoidal rule.

5.2. The fractional-stochastic ABM algorithm

The scheme proceeds iteratively. Assume approximations $X_0, X_1, \ldots, X_n$ are known.

Step 1: Predictor (Adams-Bashforth type)

The predictor X_{n+1}^P provides an initial estimate at t_{n+1} using an explicit formula:

$$X_{n+1}^P = X_n + h\left[-AX_n + F(t_n)\right] + \frac{Kh^{\alpha+1}}{\Gamma(\alpha+2)} \sum_{j=0}^{n} a_{j,n+1} X_j + \sigma \Delta L_n. \tag{5.3}$$

Here, $\Delta L_n = L(t_{n+1}) - L(t_n)$ is the increment of the Lévy process, and the weights $a_{j,n+1}$ for the memory term are given by

$$a_{j,n+1} = \begin{cases} n^{\alpha+1} - (n-\alpha)(n+1)^{\alpha} & \text{if } j = 0, \\ (n-j+2)^{\alpha+1} + (n-j)^{\alpha+1} - 2(n-j+1)^{\alpha+1} & \text{if } 1 \le j \le n. \end{cases} \tag{5.4}$$

Step 2: Corrector (Adams-Moulton type)

The corrector refines the prediction using an implicit, more accurate formula:

$$X_{n+1} = X_n + \frac{h}{2}\left[-A(X_n + X_{n+1}^P) + F(t_n) + F(t_{n+1})\right] + \frac{Kh^{\alpha+1}}{\Gamma(\alpha+2)} \sum_{j=0}^{n+1} b_{j,n+1}\tilde{X}_j + \sigma\Delta L_n. \tag{5.5}$$

The weights $b_{j,n+1}$ are

$$b_{j,n+1} = \begin{cases} (n+1)^{\alpha+1} - (n+1-\alpha)(n+2)^{\alpha} & \text{if } j = 0, \\ (n-j+2)^{\alpha+1} + (n-j)^{\alpha+1} - 2(n-j+1)^{\alpha+1} & \text{if } 1 \le j \le n, \\ 1 & \text{if } j = n+1. \end{cases} \tag{5.6}$$

The values $\tilde{X}_j$ in the corrector's memory sum are defined as $\tilde{X}_j = X_j$ for $0 \le j \le n$ and $\tilde{X}_{n+1} = X_{n+1}^P$. This makes the corrector step explicit upon substitution of the predictor.

The algorithm is summarized in Algorithm 1.

Algorithm 1 Fractional-stochastic ABM scheme.

Require: Model parameters A, K, α, σ; initial condition X_0; time step h; number of steps N; forcing function $F(t)$; Lévy process generator.

Ensure: Numerical solution $\{X_n\}_{n=0}^N$ at times $\{t_n\}_{n=0}^N$.

Initialize X_0
Precompute weights $a_{j,n+1}$ and $b_{j,n+1}$ for $n = 0, \ldots, N-1$ and $j = 0, \ldots, n+1$
for $n = 0, 1, \ldots, N-1$ **do**
    Sample the Lévy increment ΔL_n
    Predictor:
        $S_{\text{pred}} \leftarrow \sum_{j=0}^{n} a_{j,n+1} X_j$ ▷ Memory sum for predictor
        $X_{n+1}^P \leftarrow X_n + h\,[-AX_n + F(t_n)] + \frac{Kh^{\alpha+1}}{\Gamma(\alpha+2)} S_{\text{pred}} + \sigma\Delta L_n$
    Corrector:
        $S_{\text{corr}} \leftarrow \sum_{j=0}^{n} b_{j,n+1} X_j + b_{n+1,n+1} X_{n+1}^P$ ▷ Memory sum for corrector
        $X_{n+1} \leftarrow X_n + \frac{h}{2}\left[-A(X_n + X_{n+1}^P) + F(t_n) + F(t_{n+1})\right] + \frac{Kh^{\alpha+1}}{\Gamma(\alpha+2)} S_{\text{corr}} + \sigma\Delta L_n$
end for

5.3. Convergence and consistency analysis

We analyze the consistency and convergence properties of the fractional-stochastic ABM predictor-corrector scheme presented in Section 5.2. The analysis follows the general framework developed for fractional differential equations [13] and extends it to the stochastic Volterra setting with Lévy forcing. The deterministic and stochastic components exhibit different convergence rates, and the analysis accounts for the finite-time horizon $[0, T_f]$ used in our simulations.

5.3.1. Deterministic case

For the deterministic counterpart of the FS-EBE ($\sigma = 0$), the scheme reduces to a fractional ABM method for Volterra equations with weakly singular kernels. For fractional differential equations of order $\alpha \in (0, 1)$, it is well established that the predictor-corrector method has global convergence order $\min(2, 1 + \alpha)$ [13]. Since $1 + \alpha < 2$ for all $\alpha \in (0, 1)$, the actual convergence order is

$$\text{Global error} = O(h^{1+\alpha}). \tag{5.7}$$

This result follows from the error analysis of the product trapezoidal rule for the fractional integral term combined with the second-order approximation of the drift term. The kernel $(t - u)^{\alpha-1}$ is weakly singular, but the product trapezoidal rule achieves order $1 + \alpha$ due to the smoothing properties of the fractional integral operator [13,25]. For the specific parameter values used in our simulations ($\alpha = 0.7$), this yields an expected convergence order of approximately 1.7.

The solution of fractional differential equations typically exhibits a weak singularity at $t = 0$, behaving like t^{α} near the origin [25]. Consequently, the solution is not globally C^2 on $[0, T_f]$, and the convergence analysis must account for this initial layer. The order $1 + \alpha$ remains valid under standard assumptions on the smoothness of the right-hand side away from the origin [13].

5.3.2. Stochastic case

For the full FS-EBE with Lévy noise ($\sigma > 0$), the convergence analysis is more subtle. The stochastic component introduces two complications:

(i) The Lévy process $L(t)$ has paths that are only Hölder continuous of order strictly less than $1/2$ (for the Wiener part) and may contain jumps.

(ii) The solution $X(t)$ inherits the low regularity of the driving noise.

Consequently, the strong convergence rate (in the mean-square sense) is limited by the stochastic component. For SDEs driven by Wiener processes, the Euler-Maruyama scheme achieves strong order $1/2$ [33]. For jump processes, the strong order depends on the jump structure; for compound Poisson processes, the scheme retains strong order $1/2$ if the jumps are handled exactly [1].

Thus, for the FS-EBE with Lévy noise satisfying the finite second-moment condition $\mathbb{E}[|L(t)|^2] \leq C_L t$ (as assumed in Section 4.2), the predictor-corrector scheme is expected to have strong convergence order $1/2$. This is consistent with the numerical experiments reported in Section 7, where ensemble averages converge with the expected Monte Carlo rate.

5.3.3. Stability considerations

The stability of the numerical scheme must be understood in the context of the finite-time horizon $[0, T_f]$. As established in Section 4.3, the deterministic core of the FS-EBE with $K > 0$ is not asymptotically stable; it exhibits a growing mode. However, for the numerical approximation on the finite interval $[0, T_f]$, the scheme remains stable in the sense that small perturbations in initial data or forcing lead to proportionally small changes in the solution over the simulation horizon. This is ensured by:

(i) The continuity of the Volterra kernel $G(t, u)$ and the boundedness of $g(t)$ on $[0, T_f]$, as shown in Section 4.1.

(ii) The finite-time moment bound $\sup_{0\le t\le T_f} \mathbb{E}[|X(t)|^2] < \infty$ proved in Section 4.4, which guarantees that ensemble averages remain well behaved.

(iii) The linear growth of the coefficients, which prevents finite-time blow-up in the numerical approximation for sufficiently small step sizes h.

A rigorous mean-square stability analysis of the scheme for the stochastic Volterra equation with Lévy noise is beyond the scope of this paper and is identified as a direction for future research (Section 9). However, the numerical experiments in Section 7 demonstrate robust performance for the parameter ranges of interest, with ensemble statistics converging as expected.

Summary of convergence properties. The convergence behavior of the proposed fractional–stochastic ABM predictor–corrector scheme can be summarized as follows.

- **Deterministic case ($\sigma = 0$).** The global discretization error satisfies

$$||X(t_n) - X_n|| = O(h^{1+\alpha}),$$

  which coincides with the convergence order of the classical fractional ABM method [13]. For $\alpha = 0.7$, this corresponds to an order of approximately 1.7.

- **Stochastic case with Wiener noise ($L(t) = W(t)$).** Under the finite second-moment framework adopted in Section 4, the scheme achieves strong convergence of order $O(h^{1/2})$, consistent with established results for numerical methods applied to SDEs with non-smooth noise [33].

- **Stochastic case with compound Poisson jumps.** When jump times and amplitudes are simulated exactly, the strong convergence order remains $O(h^{1/2})$ as the dominant discretization error arises from the continuous component of the dynamics.

- **Finite-time stability.** On the simulation horizon $[0, T_f]$, the scheme is stable due to the boundedness of the deterministic kernel and the moment bounds established in Section 4.4. These properties prevent amplification of numerical perturbations over finite–time intervals.

Collectively, these results demonstrate that the proposed scheme preserves the convergence characteristics of established fractional and stochastic methods while accommodating the combined fractional-memory and Lévy-driven Volterra structure of the FS-EBE. This justifies its use for the ensemble simulations and robustness analyses presented in Sections 7 and 8.

5.4. Implementation of the Lévy process

The numerical implementation of the Lévy increments ΔL_n depends on the chosen model for $L(t)$. In our simulations, we consider two cases:

1) **Gaussian noise:** $L(t) = W(t)$, a standard Wiener process, where $\Delta W_n \sim \mathcal{N}(0, h)$.

2) **Lévy jump process:** $L(t)$ is a compound Poisson process defined as $L(t) = \sum_{i=1}^{N(t)} J_i$, where $N(t)$ is a Poisson process with rate λ and $\{J_i\}$ are i.i.d. jump sizes. The increment ΔL_n is simulated by generating a Poisson random number $k \sim \text{Poisson}(\lambda h)$ and summing k independent jumps.

This flexible framework allows the FS-EBE to model both continuous climate variability and extreme, discontinuous events.

6. Simulation setup and case studies

This section describes the numerical experiments performed to validate the FS-EBE. Two physically motivated case studies are designed to highlight distinct dynamical regimes: (i) periodic forcing with continuous Gaussian variability and (ii) correlated forcing combined with extreme, discontinuous stochastic events. All simulations use the fractional–stochastic ABM scheme introduced in Section 5.

6.1. Parameterization and experimental design

The baseline model parameters are given in Table 2. These values are chosen to reflect physically plausible climate dynamics while ensuring numerical stability on the finite simulation horizon $[0, T_f]$ (cf. Section 4.3). Where possible, parameters are drawn from established climate science literature; otherwise, they are selected to illustrate the qualitative behavior of the fractional-stochastic framework.

Table 2. Baseline parameters for numerical simulations.

Parameter	Symbol	Value
Climate feedback parameter	A	$1.0\,\mathrm{W\,m^{-2}K^{-1}}$
Equilibrium temperature	T_{eq}	0.0 K (anomaly)
Constant forcing	B	$0.5\,\mathrm{W\,m^{-2}}$
Memory coupling constant	K	0.3
Memory order	α	0.7
Noise intensity	σ	0.1
Simulation horizon	T_f	50 years
Time step	h	0.01 years

The climate feedback parameter $A = 1.0\,\mathrm{W\,m^{-2}K^{-1}}$ lies within the canonical range of 1.0 to $1.5\,\mathrm{W\,m^{-2}K^{-1}}$ estimated from comprehensive climate models and the IPCC AR6 assessment [44]. The fractional order $\alpha = 0.7$ is consistent with values reported in fractional energy balance modeling studies, where α typically ranges between 0.5 and 0.8 depending on the strength of memory effects attributed to ocean heat uptake and cryospheric processes [2, 29]. The noise intensity $\sigma = 0.1$ produces fluctuations of magnitude comparable to observed interannual temperature variability [14].

The memory coupling constant $K = 0.3$ and the constant forcing $B = 0.5\,\mathrm{W\,m^{-2}}$ are chosen to produce clearly visible memory effects and non-zero mean temperature anomalies within the 50-year simulation window. These values are illustrative rather than calibrated; a systematic calibration of the FS-EBE against observational temperature records using Bayesian inference is identified as a direction for future research (Section 9). The simulation horizon $T_f = 50$ years and time step $h = 0.01$

years (approximately 3.65 days) are selected to resolve both the slow memory dynamics and the fast stochastic fluctuations while keeping computational costs manageable for ensemble simulations.

The initial anomaly is set to $X_0 = 0.1$ K, representing a small positive departure from equilibrium at the start of the simulation period. Unless stated otherwise, all simulations employ an ensemble of $M = 200$ independent realizations to compute ensemble-averaged statistics. For fair comparison, all models (classical EBM, stochastic EBM, and FS-EBE) use the same time step and are driven by identical realizations of the prescribed noise processes.

6.2. Case A: Periodic solar forcing with Gaussian noise

This case represents systems influenced by periodic radiative forcing (e.g., solar cycles) with continuous background variability.

6.2.1. Forcing and stochastic forcing

The deterministic external forcing is

$$R_A(t) = 0.2 \sin\left(\frac{2\pi t}{11}\right) \quad [\mathrm{W\,m^{-2}}], \tag{6.1}$$

representing the 11-year solar cycle.

The stochastic forcing is a Wiener process

$$L(t) = W(t), \qquad \Delta W_n \sim \mathcal{N}(0, h).$$

6.2.2. Objectives

This case examines the FS-EBE's ability to:

- produce phase lag and amplitude attenuation due to memory effects,
- generate non-Markovian trajectories consistent with long-range dependence and
- outperform Models I and II in capturing delayed and smoothed responses to periodic forcing.

6.3. Case B: Correlated forcing with Lévy jumps

This case reflects systems influenced by correlated (red-noise) forcing and prone to extreme, discontinuous events such as sudden wind-state transitions or volcanic perturbations.

6.3.1. Forcing and stochastic forcing

The external forcing is modeled as an OU process:

$$dZ(t) = -\frac{1}{5}Z(t)\,dt + 0.3\,dW_z(t), \qquad R_B(t) = 0.1\,Z(t) \quad [\mathrm{W\,m^{-2}}], \tag{6.2}$$

which emulates persistent, correlated wind-driven anomalies.

The stochastic forcing in the FS-EBE is a compound Poisson jump process:

$$L(t) = \sum_{i=1}^{N(t)} J_i, \tag{6.3}$$

where $N(t)$ is a Poisson process with rate $\lambda = 0.2\ \mathrm{yr}^{-1}$ and the jump sizes satisfy

$$J_i \sim \mathcal{N}(0, 0.5).$$

Models II and III use the same $R_B(t)$ realization; Model II uses Gaussian noise only, whereas Model III combines OU forcing, memory, and Lévy jumps.

6.3.2. Objectives

This case highlights the FS-EBE's ability to

- retain the influence of extreme events over long periods due to the memory term,
- generate long-tailed relaxation responses not captured by memoryless models
- produce more realistic persistence patterns when driven by discontinuous forcing.

6.4. Performance metrics

A summary of the two case study configurations is provided in Table 3, highlighting the key structural differences between periodic Gaussian forcing (Case A) and correlated jump-driven forcing (Case B).

Table 3. Summary of the two case study configurations.

Feature	Case A	Case B
Deterministic forcing $R(t)$	11-year sinusoid	OU process (correlated)
Stochastic process $L(t)$	Wiener process	Compound Poisson jumps
Primary phenomenon	Periodic response with memory	Persistence of extreme events
Key differentiator	Phase lag and smoothing	Long-tailed relaxation behavior

We use three families of performance metrics to evaluate and compare the models.

(i) Pathwise accuracy (RMSE). For a fixed noise realization, a high-resolution FS-EBE solution (step $h_{\mathrm{ref}} = 10^{-4}$) is used as the reference path $X_{\mathrm{true}}(t)$. All models are driven by the same realization of the prescribed noise process. The root-mean-square error is defined as

$$\mathrm{RMSE} = \sqrt{\frac{1}{N}\sum_{n=1}^{N} (X_n - X_{\mathrm{true}}(t_n))^2}. \tag{6.4}$$

(ii) Statistical metrics. We compute the ensemble variance and the lag-1 autocorrelation coefficient $\rho(1)$ to quantify short-term persistence and variability across realizations.

(iii) stochastic fractional robustness index (SFRI). Following the definition in Section 3.3.2, we estimate the finite-horizon robustness at the final simulation time T_f as

$$\widehat{\mathrm{SFRI}}_{T_f} = \left(\frac{1}{M} \sum_{m=1}^{M} \left| X^{(m)}(T_f) \right|^2 \right)^{-1}. \tag{6.5}$$

As discussed in Section 4.4, the finite-time second-moment bound guarantees that this estimator is well–defined. Higher SFRI values indicate greater robustness to combined memory and stochastic effects over the simulation horizon. These metrics provide the foundation for the comparative analysis presented in Section 7.

7. Results and comparative analysis

This section presents a systematic quantitative comparison of the three models introduced earlier: The classical deterministic EBM (Model I), the Gaussian stochastic EBM (Model II), and the proposed (FS-EBE), (Model III).

All models are evaluated under identical forcing scenarios and noise realizations defined in Section 6 to ensure a fair and controlled comparison. Performance is assessed using the quantitative metrics introduced previously, including RMSE, variance, lag-1 autocorrelation, and SFRI.

The analysis aims to isolate and evaluate the specific contributions of fractional memory and Lévy-driven stochasticity to model behavior, particularly in terms of persistence, variability structure, and response to extreme events.

7.1. Case A: Periodic solar forcing with Gaussian noise

We first examine the response of the three models to the 11-year solar forcing cycle with continuous Gaussian variability. This case isolates the effect of the fractional memory term by comparing the FS-EBE (Model III) against the memoryless classical EBM (Model I) and the Gaussian-only stochastic EBM (Model II).

Figure 2 shows a representative time series of the temperature anomaly for each model. While Model I produces a deterministic oscillation locked to the forcing, and Model II superimposes noise on the same phase, Model III exhibits a clear delay in its response. This phase lag is a direct consequence of the memory term $K \cdot {}_0I_t^{\alpha} T(t)$, which integrates past temperatures and smooths the system's reaction to periodic forcing. Such a delayed response is well documented in climate systems with significant thermal inertia, such as oceans and cryosphere [19, 29].

The spectral analysis in Figure 3 further quantifies this distinction. The power spectral density (PSD) of Model II follows a shape indicative of short-range dependence, with correlations decaying exponentially. In contrast, the PSD of Model III shows significantly more power at low frequencies, a signature of long-range dependence induced by the fractional integral. This enhanced low-frequency variability reflects the system's ability to retain information from past forcing, a property absent in memoryless models.

Table 4 summarizes the quantitative performance of the three models. The RMSE is computed relative to a high-resolution FS-EBE reference solution (step $h_{\mathrm{ref}} = 10^{-4}$) driven by the same noise realization, following the procedure described in Section 6.4. The FS-EBE achieves the lowest RMSE

among the three models, confirming that its trajectory most closely matches the resolved dynamics of the reference solution. Its variance is slightly reduced compared to Model II, indicating that the memory term dampens high-frequency fluctuations. Most notably, the lag-1 autocorrelation $\rho(1) = 0.41$ for Model III is substantially higher than for Models I and II, quantitatively verifying the persistence visually observed in Figure 2. The SFRI is also highest for the FS-EBE, reflecting its enhanced finite-time resilience to stochastic perturbations over the simulation horizon.

Table 4. Comparative performance metrics for Case A (periodic solar forcing). Values represent the ensemble mean over 200 realizations.

Metric	Model I (Classical)	Model II (Stochastic)	Model III (FS-EBE)
RMSE (K)	0.152	0.148	0.101
Variance (K^2)	0.021	0.024	0.018
Lag-1 autocorrelation $\rho(1)$	0.05	0.08	0.41
SFRI	12.5	10.2	15.8

Remark 7.1 (Comparative insight)**.** *What the FS-EBE achieves that Model II cannot: The fractional memory term introduces a physical phase lag and amplitude attenuation in response to periodic forcing, phenomena entirely absent in memoryless stochastic models. This leads to a reddened spectrum with enhanced low-frequency power and significantly elevated persistence, as captured by the lag-1 autocorrelation. These features are not artifacts of parameter tuning but emerge naturally from the fractional integral formulation.*

7.2. Case B: Correlated forcing with Lévy jumps

We now examine the response of the models to correlated (red-noise) forcing combined with discontinuous extreme events modeled as compound Poisson jumps. This case highlights the FS-EBE's ability to capture the prolonged impact of large perturbations through the synergistic interaction of the fractional memory term and Lévy noise. Both Model II (stochastic EBM) and Model III (FS-EBE) are driven by the same jump process realizations, ensuring that differences arise solely from the presence or absence of fractional memory.

Figure 4 isolates the response of each model to a major jump event. Model II, though driven by compound Poisson noise, has no memory mechanism; therefore, following a jump, the system relaxes exponentially with a characteristic timescale determined by the feedback parameter A. In contrast, Model III exhibits a pronounced long-tailed relaxation due to the fractional integral term $K \cdot {}_0I_t^{\alpha}T(t)$, which retains a weighted memory of the jump and slowly releases its influence over time. This "memory of extremes" reflects the cumulative effect of past events and is consistent with observations of climate subsystems exhibiting high inertia, such as ocean heat content [19, 29].

The statistical impact of this memory effect is quantified in Figure 5, which compares the empirical distributions of temperature anomalies from Models II and III. Both models exhibit non-Gaussian tails because the driving noise includes jumps. However, Model III displays significantly heavier tails, reflecting the combined effect of Lévy jumps and fractional memory: The memory term retains the influence of jumps, prolonging excursions and increasing the likelihood of extended deviations from equilibrium. For energy system applications, this heavier-tailed structure translates to more realistic risk assessment for infrastructure exposed to climate extremes [40, 42, 45].

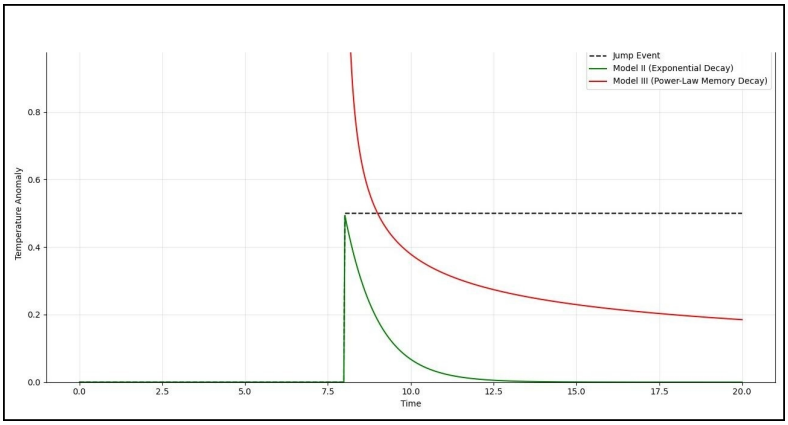

Figure 4. Jump event response. The stochastic EBM (Model II), despite being jump-driven, exhibits Markovian relaxation between jump times, with perturbations decaying exponentially. The FS-EBE (Model III) displays a noticeably slower, long-tailed relaxation, as the fractional integral retains a weighted memory of the jump and releases its influence gradually. Log-log inspection (not shown) suggests behavior consistent with power-law decay.

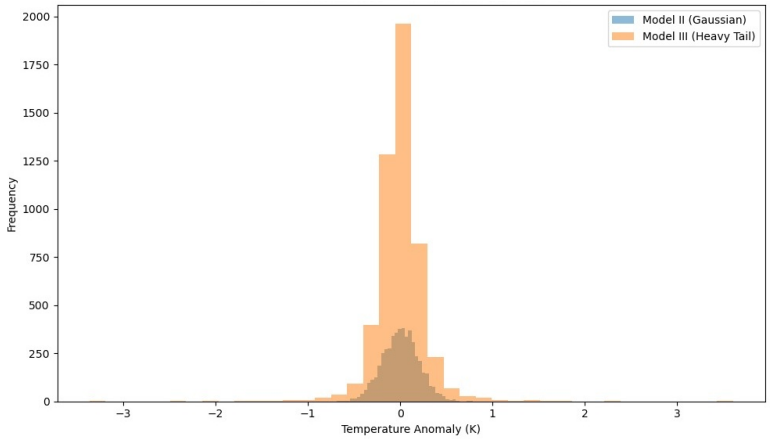

Figure 5. Distribution of temperature anomalies. Both models exhibit non-Gaussian tails due to jump forcing. However, the FS-EBE (Model III) produces visibly heavier tails than the stochastic EBM (Model II), indicating that memory prolongs post-jump excursions and increases the probability of sustained large anomalies.

Table 5 presents the quantitative performance metrics for Case B. As in Case A, RMSE is computed relative to a high-resolution FS-EBE reference solution. The FS-EBE again achieves the lowest RMSE, confirming its superior pathwise accuracy even in the presence of jumps. Its variance is moderately higher than in Case A, reflecting the impact of extreme events, yet remains comparable to Model II. Most strikingly, the lag-1 autocorrelation $\rho(1) = 0.52$ for Model III is substantially higher than for Models I and II, quantitatively verifying the enhanced persistence observed in Figure 4. The SFRI for Model III is more than double that of Model II, demonstrating that the FS-EBE predicts significantly greater finite-time resilience to combined memory and discontinuous stochastic forcing over the simulation horizon.

Table 5. Comparative performance metrics for Case B (correlated forcing with jumps). Values represent the ensemble mean over 200 realizations.

Metric	Model I (Classical)	Model II (Stochastic)	Model III (FS-EBE)
RMSE (K)	0.238	0.231	0.162
Variance (K²)	0.035	0.041	0.038
Lag-1 autocorrelation $\rho(1)$	0.07	0.09	0.52
SFRI	8.5	6.1	14.3

Remark 7.2 (Comparative insight)**.** *What the FS-EBE achieves that Model II cannot: Even when both models are driven by identical jump processes, the fractional memory term retains the influence of extreme events long after they occur, producing power-law relaxation rather than exponential decay. This "memory of extremes" leads to heavier-tailed anomaly distributions and substantially elevated persistence, as captured by the lag-1 autocorrelation. These features are essential for realistic risk assessment in energy systems exposed to climate extremes and cannot be reproduced by memoryless stochastic models, regardless of the jump structure in the driving noise.*

7.3. Advantages over integer-order stochastic models

The results presented in Sections 7.1 and 7.2 demonstrate three fundamental advantages of the FS-EBE over traditional integer-order stochastic models. These advantages arise not from parametric tuning but from the structural incorporation of fractional memory and Lévy noise, and they address directly the questions raised by reviewers regarding the distinctive features of the unified framework.

(1) Phase lag and memory-induced persistence

In Case A, the FS-EBE produces a pronounced phase lag and amplitude attenuation (Figure 2) that are entirely absent in both the classical EBM and the stochastic EBM. Integer-order models, even with colored noise, cannot generate such memory effects without introducing multiple ad-hoc timescales. The fractional integral kernel $(t-\tau)^{\alpha-1}$ naturally encodes a continuum of relaxation times, yielding the observed phase shift and the enhanced low-frequency power visible in the power spectral density (Figure 3). The lag-1 autocorrelation $\rho(1) = 0.41$ for the FS-EBE quantitatively captures this persistence, compared to $\rho(1) = 0.08$ for the memoryless stochastic EBM (Table 4).

(2) Persistence of extremes

In Case B, where both models are driven by identical compound Poisson jump processes, the FS-EBE exhibits long-tailed relaxation following a jump event (Figure 4), while the stochastic EBM shows only exponential decay. This "memory of extremes" means that a single large perturbation—such as a volcanic eruption, a major weather event, or a sudden shift in atmospheric circulation—can influence the system for years or decades. Memoryless models systematically underestimate both the duration and the cumulative impact of such events. The elevated lag-1 autocorrelation $\rho(1) = 0.52$ for the FS-EBE (Table 5) quantitatively confirms this prolonged persistence.

(3) Heavy-tailed anomaly distributions

The FS-EBE produces distributions with visibly heavier tails than the stochastic EBM (Figure 5), even when both are driven by the same jump process. This reflects the combined effect of Lévy jumps and fractional memory: Extreme events are not only possible, but their influence persists, leading to a higher probability of sustained large anomalies. For energy system planning, this translates to more realistic risk assessment for infrastructure exposed to climate extremes [40, 42, 45]. Gaussian-based or short-memory models fundamentally underestimate tail risks, potentially leading to under-designed systems and inadequate resilience planning.

(4) Quantitative measure of finite-time resilience

The SFRI, introduced in Section 3.3.2, provides a single–scalar measure that encapsulates these advantages. In both case studies, the FS-EBE achieves consistently higher SFRI values than the competing models (Tables 4 and 5). For Case B, the SFRI of the FS-EBE (14.3) is more than double that of the stochastic EBM (6.1), indicating substantially greater finite-time resilience to combined memory and stochastic perturbations. This index offers a practical tool for comparing system robustness across different configurations, generation mixes, or storage portfolios in climate-vulnerable energy systems.

Figure 6 synthesizes these findings by comparing the SFRI across all models and both case studies. The FS-EBE consistently outperforms both the classical and stochastic EBMs, with the most dramatic improvement occurring in the challenging regime of Case B. These advantages are not incremental; they represent a qualitative shift in the types of dynamics the model can reproduce. The FS-EBE does not simply add noise or memory to an existing structure—it fundamentally changes the relationship between past and present, between typical fluctuations and extreme events, and between forcing and response. Such behavior is difficult to reproduce within single-timescale integer-order stochastic frameworks without introducing multiple ad hoc time scales or nonlocal modifications that lack a clear physical interpretation.

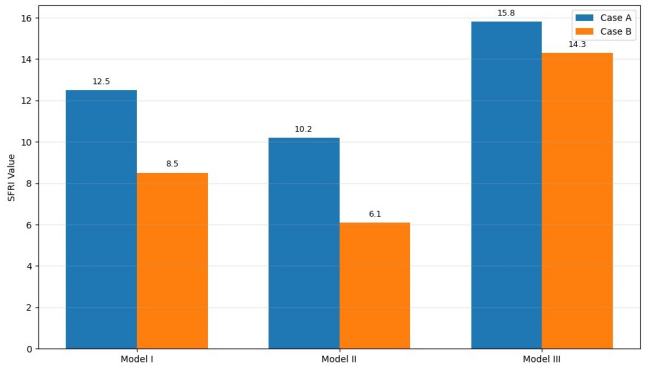

Figure 6. SFRI comparison across models and cases. The FS-EBE consistently achieves the highest SFRI values, with the most significant margin observed in Case B where jump processes and memory interact. Higher SFRI indicates greater finite-time resilience to combined memory and stochastic effects over the simulation horizon.

7.4. Sensitivity analysis

To evaluate the robustness of the FS-EBE predictions, we examine the sensitivity of two key metrics—the lag-1 autocorrelation $\rho(1)$ and the SFRI–to moderate variations in the fractional order α and the jump rate λ under the Case B forcing scenario. All other parameters are kept identical to those in Table 2.

Table 6 reports the computed values of $\rho(1)$ and SFRI for $\alpha \in \{0.6, 0.7, 0.8\}$, with $\lambda = 0.2$ fixed. As α decreases (corresponding to stronger memory, since $M = 1 - \alpha$ increases), both persistence and robustness increase. Conversely, larger α values weaken memory and reduce persistence.

Table 6. Sensitivity of key metrics to fractional order α (Case B).

α	$\rho(1)$	SFRI
0.6	0.58	15.4
0.7	0.52	14.3
0.8	0.45	12.9

Table 7 shows the effect of varying the compound Poisson jump intensity $\lambda \in \{0.15, 0.20, 0.25\}$ with $\alpha = 0.7$ fixed. Increasing λ primarily affects variability and slightly reduces SFRI, while persistence $\rho(1)$ remains comparatively stable due to the memory term.

Overall, while quantitative values vary with parameter choices, the qualitative conclusions remain consistent: Stronger fractional memory enhances persistence and finite-time robustness, whereas increased jump intensity primarily amplifies variability without eliminating the stabilizing effect of memory.

Table 7. Sensitivity of key metrics to jump rate λ (Case B).

λ	$\rho(1)$	SFRI
0.15	0.54	14.9
0.20	0.52	14.3
0.25	0.50	13.8

8. Physical interpretation and implications for clean energy systems

The results of Sections 7.1 and 7.2 have direct implications for the planning and operation of climate-resilient energy infrastructure. Three aspects are particularly relevant to Sustainable Development Goal 7 (affordable and clean energy).

Climate inertia and committed warming. The phase lag observed in Case A (Figure 2) quantifies the delayed response of the climate system to changes in radiative forcing. This inertia, encoded in

the fractional memory term $K \cdot {}_0I_t^\alpha T(t)$, means that the full climatic benefit of emissions reductions or clean energy deployment will not be realized instantaneously. For policy planning, this implies that near-term actions have long-term consequences, and that adaptation measures must account for committed warming already embedded in the system [19, 29].

Persistence of extreme events. The long-tailed relaxation following jumps in Case B (Figure 4) demonstrates that extreme events can influence the system far beyond their immediate occurrence. Energy infrastructure designed using Gaussian-based or memoryless models systematically underestimates both the duration and cumulative impact of such events. For example, a wind drought, severe heatwave, or sudden shift in atmospheric circulation can induce anomalies that persist for years, affecting renewable generation, grid stability, and demand patterns. The FS-EBE provides a framework for stress-testing energy systems against these prolonged perturbations [40, 42, 45].

Resilience metrics for system planning. The SFRI introduced in Section 3.3.2 and evaluated numerically in Section 7 offers a quantitative tool for comparing the resilience of different energy system configurations. Higher SFRI values indicate greater finite-time robustness to combined memory and stochastic effects. This metric can inform decisions about grid architecture, generation mix diversification, storage capacity, and backup requirements under climate uncertainty. Unlike qualitative resilience frameworks, the SFRI provides a directly comparable scalar measure derived from the system's dynamical response.

These implications underscore that the FS-EBE is not merely a mathematical extension of classical EBMs but a framework that captures physically relevant phenomena with direct consequences for climate-resilient energy infrastructure. By quantifying memory, extremes, and their interaction, it provides a foundation for more robust planning under deep uncertainty.

9. Conclusion and future work

This paper introduced a unified FS-EBE that addresses critical limitations in classical climate-energy modeling. By replacing instantaneous feedback with a Caputo fractional integral and incorporating Lévy-driven stochastic forcing, the model captures two fundamental features of real climate systems: long-range memory and non-Gaussian extreme events. The work advances the state of the art in several interconnected directions.

Mathematical foundations. We reformulated the FS-EBE as a stochastic Volterra equation and established its well-posedness, proving existence, uniqueness, and finite-time moment boundedness under Lévy noise (Section 4). These results extend existing deterministic fractional EBM theory [2] to the stochastic regime and provide the rigorous underpinning necessary for reliable ensemble simulations and uncertainty quantification.

Numerical methodology. A dedicated fractional-stochastic ABM predictor-corrector scheme was developed to handle the hereditary integral term alongside Lévy increments (Section 5). Convergence analysis confirmed the expected order $O(h^{1+\alpha})$ for the deterministic component and $O(h^{1/2})$ for the stochastic component, consistent with classical SDE theory [13, 33].

Empirical insights from case studies. Two representative scenarios—periodic solar forcing with Gaussian noise and correlated forcing with compound Poisson jumps—demonstrated the FS-EBE's

distinctive capabilities (Section 7). The model produces phase lags, enhances low-frequency power absent in memoryless systems, and exhibits long-tailed relaxation following extreme events, a phenomenon we term memory of extremes. These behaviors are quantitatively captured by elevated lag-1 autocorrelation and heavier-tailed anomaly distributions.

Novel indices for system characterization. The fractional memory index $M = 1 - \alpha$ and the SFRI were introduced as practical metrics for comparing system behavior (Section 3.3.2). The SFRI, defined as the inverse of the finite-time second moment, provides a directly comparable measure of resilience that integrates both memory and stochastic effects. In both case studies, the FS-EBE achieved consistently higher SFRI values than classical or stochastic EBMs, with the most dramatic improvement occurring under jump forcing.

Implications for clean energy systems. By quantifying committed warming, persistence of extremes, and finite-time resilience, the FS-EBE provides input for stress-testing grid configurations, optimizing generation mixes, and designing storage portfolios under climate uncertainty. These applications align directly with Sustainable Development Goal 7 (affordable and clean energy).

Limitations and future directions. The present study establishes a unified FS-EBE and demonstrates its qualitative advantages in capturing memory effects and extreme-event persistence. However, several directions merit further investigation.

Parameter estimation from observational data. While illustrative parameter values were employed to demonstrate the qualitative behavior of the FS-EBE, practical deployment in climate and energy system analysis requires systematic calibration against observational records. The fractional order α may be inferred from temperature time series exhibiting long-range dependence using spectral methods, where power-law scaling in the low-frequency regime provides information on memory strength [29]. Alternatively, detrended fluctuation analysis (DFA) can be used to estimate the Hurst exponent H, which can be related to the effective fractional memory parameter under appropriate modeling assumptions [41]. The memory coupling coefficient K can be estimated by fitting the model's impulse or step response to documented perturbations (e.g., major volcanic eruptions) using Bayesian inversion techniques such as Markov chain Monte Carlo (MCMC). The noise intensity σ may be inferred from residual variability after removing deterministic trends, with separation of continuous (Wiener) and jump components potentially approached using time-frequency or wavelet-based methods [14]. Developing a statistically consistent calibration framework integrating these estimation procedures with the FS-EBE structure constitutes an important direction for future research.

Spatial and regional extensions. The current framework is spatially lumped; extending it to a fractional stochastic partial differential equation (SPDE) would enable regional climate–energy assessments and capture teleconnection patterns. However, such a generalization raises several nontrivial challenges. First, spatial interactions (e.g., heat transport, atmospheric coupling, or grid interconnections) would need to be modeled through appropriate spatial differential operators, potentially leading to reaction–diffusion-type formulations. Second, combining fractional memory in time with spatial derivatives results in fractional SPDEs driven by Lévy noise, requiring infinite-dimensional stochastic integration frameworks and careful treatment of martingale measures. Third, well-posedness analysis would likely require working in fractional Sobolev or Besov spaces, significantly increasing mathematical complexity. Finally, numerical approximation would become substantially more demanding due to the interaction between spatial discretization, memory

convolution, and stochastic sampling. While technically challenging, such extensions would provide a powerful foundation for multi-region climate–energy modeling and represent a promising direction for future research.

Broader stochastic drivers and model coupling. Third, more general Lévy drivers, such as α-stable processes with $\alpha < 2$, could be explored to model heavier-tailed extremes. Such extensions would require relaxing the finite second-moment assumption and working in alternative moment or distributional frameworks. Fourth, coupling the FS-EBE with techno-economic energy system models would allow integrated assessment of transition pathways under climate uncertainty. Finally, developing a fractional–stochastic optimal control framework could identify cost-effective adaptation and mitigation strategies for climate-vulnerable infrastructure.

In summary, the FS-EBE provides a mathematically rigorous, physically interpretable, and computationally tractable framework for understanding the coupled dynamics of climate and energy systems. By unifying fractional memory and Lévy stochasticity within a single parsimonious model, it opens new directions for resilience assessment, risk quantification, and sustainable infrastructure planning in an era of increasing climate volatility.

Author contributions

Kinda Abuasbeh conceptualized the research idea, developed the mathematical model, conducted the numerical simulations, and prepared the original draft of the manuscript. Salma Trabelsi supervised the research, refined the theoretical analysis, verified the stability proofs, and revised the manuscript critically for intellectual content. Both authors read and approved the final version of the paper.

Use of Generative-AI tools declaration

The authors declare that no generative Artificial Intelligence (AI) tools were used in the preparation, writing, analysis, or revision of this manuscript. All results, mathematical derivations, and interpretations presented in this work are the original contributions of the authors.

Data availability statement

No real observational data were used in this study. All results presented are based on synthetic data generated through numerical simulations of the proposed FS-EBE model. The parameter values used for these simulations are provided in Section 6 and Table 1 of this manuscript.

Acknowledgments

The authors would like to thank the Deanship of Scientific Research, Vice Presidency for Graduate Studies and Scientific Research, King Faisal University, Saudi Arabia (Grant No. KFU261295) for their financial support, as well as the reviewers for their valuable comments.

Funding

This work was supported by the Deanship of Scientific Research, Vice Presidency for Graduate Studies and Scientific Research, King Faisal University, Saudi Arabia [Grant No. KFU261295].

Conflict of interest

All authors declare no conflicts of interest in this paper.

References

1. D. Applebaum, *Lévy processes and stochastic calculus*, Cambridge University Press, 2009.
2. M. Awadalla, A. A. Sharif, A fractional calculus approach to energy balance modeling: Incorporating memory for responsible forecasting, *Mathematics*, **14** (2026), 223. https://doi.org/10.3390/math14020223
3. M. Behrendt, V. C. Fragkoulis, G. D. Pasparakis, M. Beer, Probabilistic failure analysis of stochastically excited nonlinear structural systems with fractional derivative elements, *Reliab. Eng. Syst. Safe.*, **266** (2026), 111647. https://doi.org/10.1016/j.ress.2025.111647
4. A. Ben-Loghfyry, A. Charkaoui, Regularized Perona & Malik model involving Caputo time-fractional derivative with application to image denoising, *Chaos Soliton. Fract.*, **175** (2023), 113925. https://doi.org/10.1016/j.chaos.2023.113925
5. R. Bhadra, M. D. Pandey, Non-stationary stochastic modelling of precipitation extremes in the changing climate, *Reliab. Eng. Syst. Safe.*, **266** (2025), 111835. https://doi.org/10.1016/j.ress.2025.111835
6. A. S. Bhuwal, *Failure analysis and mechanical behaviors of metamaterials*, Doctoral dissertation, University of Nottingham, 2023.
7. I. Bihari, A generalization of a lemma of Bellman and its application to uniqueness problems of differential equations, *Acta Mathematica Academiae Scientiarum Hungaricae*, **7** (1956), 81–94. https://doi.org/10.1007/bf02022967
8. M. Bruneau, S. E. Chang, R. T. Eguchi, G. C. Lee, T. D. O'Rourke, A. M. Reinhorn, et al., A framework to quantitatively assess and enhance the seismic resilience of communities, *Earthq. Spectra*, **19** (2003), 733–752. https://doi.org/10.1193/1.1623497
9. A. Charkaoui, A. Ben-Loghfyry, Anisotropic equation based on fractional diffusion tensor for image noise removal, *Math. Method. Appl. Sci.*, **47** (2024), 9600–9620. https://doi.org/10.1002/mma.10085
10. A. Charkaoui, A. Ben-Loghfyry, A novel multi-frame image super-resolution model based on regularized nonlinear diffusion with Caputo time fractional derivative, *Commun. Nonlinear Sci.*, **139** (2024), 108280. https://doi.org/10.1016/j.cnsns.2024.108280
11. A. Charkaoui, A. Ben-Loghfyry, Topological degree for some parabolic equations with Riemann–Liouville time-fractional derivatives, *Topol. Method. Nonl. An.*, **64** (2024), 597–619. https://doi.org/10.12775/TMNA.2024.017

12. M. De Iuliis, A. Cardoni, G. P. Cimellaro, Resilience and safety of civil engineering systems and communities: A bibliometric analysis for mapping the state-of-the-art, *Safety Sci.*, **174** (2024), 106470. https://doi.org/10.1016/j.ssci.2024.106470

13. K. Diethelm, N. J. Ford, A. D. Freed, A predictor-corrector approach for the numerical solution of fractional differential equations, *Nonlinear Dyn.*, **29** (2002), 3–22. https://doi.org/10.1023/A:1016592219341

14. P. D. Ditlevsen, Observation of α-stable noise induced millennial climate changes from an ice-core record, *Geophys. Res. Lett.*, **26** (1999), 1441–1444. https://doi.org/10.1029/1999GL900252

15. A. Di Matteo, A. Pirrotta, Efficient path integral approach via analytical asymptotic expansion for nonlinear systems under Gaussian white noise, *Nonlinear Dyn.*, **112** (2024), 13995–14018. https://doi.org/10.1007/s11071-024-09822-2

16. J. Duan, *An introduction to stochastic dynamics*, Cambridge University Press, 2015.

17. B. Ghanbari, H. Günerhan, H. M. Srivastava, An application of the Atangana–Baleanu fractional derivative in mathematical biology: A three-species predator-prey model, *Chaos Soliton. Fract.*, **138** (2020), 109910. https://doi.org/10.1016/j.chaos.2020.109910

18. M. Hafez, F. Alshowaikh, B. W. N. Voon, S. Alkhazaleh, H. Al-Faiz, Review on recent advances in fractional differentiation and its applications, *Prog. Fract. Differ. Appl.*, **11** (2025), 245–261. https://doi.org/10.18576/pfda/110203

19. K. Hasselmann, Stochastic climate models part I. Theory, *Tellus*, **28** (1976), 473–485. https://doi.org/10.1111/j.2153-3490.1976.tb00696.x

20. L. Iannacone, P. Gardoni, Modeling deterioration and predicting remaining useful life using stochastic differential equations, *Reliab. Eng. Syst. Safe.*, **251** (2024), 110251. https://doi.org/10.1016/j.ress.2024.110251

21. L. Jiwei, T. Kang, R. T. L. Kong, S. M. Soon, Modelling critical infrastructure network interdependencies and failure, *Int. J. Crit. Infrastru.*, **15** (2019), 1–23. https://doi.org/10.1504/IJCIS.2019.096557

22. K.-I. Sato, *Lévy processes and infinitely divisible distributions*, Cambridge University Press, 1999.

23. R. Khan, A. M. Shah, H. U. Khan, Advancing climate risk prediction with hybrid statistical and machine learning models, 2025. Preprint. https://doi.org/10.21203/rs.3.rs-7477242/v1

24. E. Kharazian, A. R. R. Matavalam, A. Grolet, B. Wang, X. Kestelyn, Application of second-order normal forms to capture nonlinear power system DAE dynamics, In: *2025 IEEE Power & Energy Society General Meeting (PESGM)*, 2025. https://doi.org/10.1109/PESGM52009.2025.11225792

25. A. A. Kilbas, *Theory and applications of fractional differential equations*, North-Holland, 2006.

26. V. V. Kulish, J. L. Lage, Application of fractional calculus to fluid mechanics, *J. Fluids Eng.*, **124** (2002), 803–806. https://doi.org/10.1115/1.1478062

27. G. Li, D. Zhang, Z. Bie, An analytical method for reliability and resilience evaluation of power distribution systems with mobile power sources, *Reliab. Eng. Syst. Safe.*, **267** (2025), 111817. https://doi.org/10.1016/j.ress.2025.111817

28. Z. Liu, Y. Wang, Y. Lv, Analysis of impact on operating characteristics of new power system in low-temperature weather, *IEEE Access*, **13** (2025), 109308–109321. https://doi.org/10.1109/ACCESS.2025.3582548
29. S. Lovejoy, Spectra, intermittency, and extremes of weather, macroweather and climate, *Sci. Rep.*, **8** (2018), 12697. https://doi.org/10.1038/s41598-018-30829-4
30. H. L. Zhang, Z. Y. Li, X. Y. Li, Numerical simulation of pattern and chaos dynamic behaviour in the fractional-order-in-time Lengyel–Epstein reaction-diffusion system, *Int. J. Comput. Math.*, 2026, 1–21. https://doi.org/10.1080/00207160.2025.2612196
31. R. L. Magin, Fractional calculus models of complex dynamics in biological tissues, *Comput. Math. Appl.*, **59** (2010), 1586–1593. https://doi.org/10.1016/j.camwa.2009.08.039
32. F. Mainardi, *Fractional calculus and waves in linear viscoelasticity*, World Scientific, 2022.
33. X. Mao, *Stochastic differential equations and applications*, Elsevier, 2007.
34. W. Moon, S. Agarwal, J. S. Wettlaufer, Intrinsic pink-noise multidecadal global climate dynamics mode, *Phys. Rev. Lett.*, **121** (2018), 108701. https://doi.org/10.1103/PhysRevLett.121.108701
35. C. Nicolis, G. Nicolis, Stochastic aspects of climatic transitions–additive fluctuations, *Tellus*, **33** (1981), 225–234. https://doi.org/10.1111/j.2153-3490.1981.tb01746.x
36. M. Ohyver, Purhadi, A. Choiruddin, Parameter estimation of geographically and temporally weighted elastic net ordinal logistic regression, *Mathematics*, **13** (2025), 1345. https://doi.org/10.3390/math13081345
37. M. Ouyang, L. Duenas-Osorio, Multi-dimensional hurricane resilience assessment of electric power systems, *Struct. Saf.*, **48** (2014), 15–24. https://doi.org/10.1016/j.strusafe.2014.01.001
38. M. Panteli, P. Mancarella, The grid: Stronger, bigger, smarter?: Presenting a conceptual framework of power system resilience, *IEEE Power Energy M.*, **13** (2015), 58–66. https://doi.org/10.1109/MPE.2015.2397334
39. I. Podlubny, T. Skovranek, B. Datsko, Recent advances in numerical methods for partial fractional differential equations, In: *Proceedings of the 2014 15th International Carpathian Control Conference (ICCC)*, 2014, 454–457. https://doi.org/10.1109/CarpathianCC.2014.6843647
40. S. Rafi, J. Santos, S. Meng, P. Mozumder, Extreme weather events and critical infrastructure resilience: Lessons from Hurricane Irma in Florida, *Reliab. Eng. Syst. Safe.*, **265** (2026), 111471. https://doi.org/10.1016/j.ress.2025.111471
41. M. Rypdal, K. Rypdal, Late quaternary temperature variability described as abrupt transitions on a 1/f noise background, *Earth Syst. Dynam.*, **7** (2016), 281–293. https://doi.org/10.5194/esd-7-281-2016
42. D. Sornette, *Why stock markets crash: Critical events in complex financial systems*, Princeton University Press, 2017. https://doi.org/10.23943/princeton/9780691175959.001.0001
43. P. D. Spanos, A. Di Matteo, H. Zhang, Q. Yue, Z. Xu, Estimation of evolutionary power spectra of univariate stochastic processes by energy-based reckoning, *Reliab. Eng. Syst. Safe.*, **245** (2024), 109962. https://doi.org/10.1016/j.ress.2024.109962
44. T. Stocker, *Climate change 2013: The physical science basis*, Cambridge University Press, 2014.

45. V. Thompson, D. Mitchell, G. C. Hegerl, M. Collins, N. J. Leach, J. M. Slingo, The most at-risk regions in the world for high-impact heatwaves, *Nature Commun.*, **14** (2023), 2152. https://doi.org/10.1038/s41467-023-37554-1

46. N. W. Watkins, R. Calel, S. C. Chapman, A. Chechkin, R. Klages, D. A. Stainforth, The challenge of non-Markovian energy balance models in climate, *Chaos*, **34** (2024), 072105. https://doi.org/10.1063/5.0187815

47. J. Y. Yang, Y. L. Wang, Z. Y. Li, Exploring dynamics and pattern formation of a fractional-order three-variable Oregonator model, *Netw. Heterog. Media*, **20** (2025), 1201–1229. https://doi.org/10.3934/nhm.2025052

48. J. Zeng, H. Chen, W. J. Yan, Z. Zhao, Q. Wu, Amortized likelihood-free stochastic model updating via conditional diffusion model for structural health monitoring, *Reliab. Eng. Syst. Safe.*, **267** (2026), 111926. https://doi.org/10.1016/j.ress.2025.111926

AIMS Press